Journal Pre-proof

A Hybrid Discrete-Finite Element model for continuous and discontinuous beam-like members including nonlinear geometric and material effects

Igor Bouckaert, Michele Godio, João Pacheco de Almeida

Please cite this article as: I. Bouckaert, M. Godio and J. Pacheco de Almeida, A Hybrid Discrete-Finite Element model for continuous and discontinuous beam-like members including nonlinear geometric and material effects. *International Journal of Solids and Structures* (2024), doi: https://doi.org/10.1016/j.ijsolstr.2024.112770.

This is a PDF file of an article that has undergone enhancements after acceptance, such as the addition of a cover page and metadata, and formatting for readability, but it is not yet the definitive version of record. This version will undergo additional copyediting, typesetting and review before it is published in its final form, but we are providing this version to give early visibility of the article. Please note that, during the production process, errors may be discovered which could affect the content, and all legal disclaimers that apply to the journal pertain.

Highlights

A Hybrid Discrete-Finite Element model for continuous and discontinuous beam-like members including nonlinear geometric and material effects

Igor Bouckaert, Michele Godio, João Pacheco de Almeida

- Novel hybrid discrete-finite formulation enabling coupling with classical FEM

- Structure modeled as an assembly of rigid blocks with contact faces

- Contact faces modeled with distributed pairs of nonlinear springs

- Benchmark validation of buckling behaviour of continuous and discrete systems

- Joint geometric and material nonlinearity validated with rocking of a flexible column

A Hybrid Discrete-Finite Element model for continuous and discontinuous beam-like members including nonlinear geometric and material effects

Igor Bouckaert[a,*], Michele Godio[b], João Pacheco de Almeida[a]

[a]*Institute of Mechanics, Materials and Civil Engineering (iMMC), UCLouvain, Place du Levant 2, Louvain-la-Neuve, 1348, Belgium;*
igor.bouckaert@uclouvain.be ; +32(0)471 73 68 70
[b]*RISE Research Institutes of Sweden, Brinellgatan 4, Borås, 504 62, Sweden*

Abstract

This paper introduces a novel formulation, called Hybrid Discrete-Finite Element (HybriD-FEM) method, for modeling one-directional continuous and discontinuous planar beam-like members, including nonlinear geometric and material effects. In this method, the structure is modeled as a series of distinct rigid blocks, connected to each other through contact pairs distributed along the interfaces. Each of those contact pairs are composed of two nonlinear multidirectional springs in series, which can represent either the deformation of the blocks themselves, or the deformation of their interface. Unlike the Applied Element Method, in which contact pairs are composed of one single spring, the current approach allows capturing phenomena such as sectional deformations or relative deformations between two blocks composed of different materials. This method shares similarities with the Discrete Element Methods in its ability to model contact interfaces between rigid or deformable units, but does not require a numerical time-domain integration scheme. More importantly, its formulation resembles that of the classical Finite Elements Method, allowing one to easily couple the latter with HybriDFEM. Following the presentation of its formulation, the method is benchmarked against analytical solutions selected from the literature, ranging from the linear-elastic response of a cantilever beam to the buckling and rocking response of continuous flexible columns, and rigid block stackings. One final example showcases the coupling of a HybriDFEM element with a linear beam finite element.

---

1. Introduction

The modeling of discontinuities is a crucial task in the field of structural mechanics. The need for accurate and reliable modeling techniques for discontinuities arises from the necessity to simulate, among others, the response of structures that are discontinuous by construction (e.g., masonry), heterogeneous structural elements (e.g., mixed structures), cracked members (e.g., reinforced concrete), or the interactions between distinct structural components (e.g., joints, structural details, etc.) or still soil-structure interactions. Discontinuities lead to the presence of interfaces, whose behaviour affects, and in some cases governs, the overall structural behaviour. To tackle this problem, many researchers have explored different modeling techniques over the years.

The Finite Element Method (FEM) (Rust, 2015; de Borst et al., 2012), which is the most widely used modeling technique among practitioners in structural analysis, classically models the structure as a continuous medium. However, when major discontinuities are present in the structure, this assumption may not be applicable. To model discontinuities, numerous FEM-based modeling techniques exist, which can be classified as either macro- or micro-modeling approaches (Munjiza and Latham, 2002). Macro-modeling employs homogenization techniques to model large portions of the structure, averaging the discontinuous behavior as an equivalent continuum (Roca et al., 2010; Cecchi and Tralli, 2012). Although computationally efficient, these methods sacrifice detail in the description of the stress and strain distributions (Roca et al., 2010). These FEM techniques cannot hence explicitly account for system discontinuities, but rather approximate them through nonlinear constitutive relations assigned to finite elements. For instance, Continuum Damage finite elements can model cracks but often consider smeared damage spread over a large portion of the structure and are limited in their ability to account for localized damage (Lourenço et al., 1998;

---

*Corresponding author

Gatta et al., 2018). More complex FEM approaches involve interface elements included in the mesh to account for strong discontinuities (Mark et al., 1993; Pegon et al., 1995; Moes et al., 1999; Zhang et al., 2017) and crack propagation in the material (Swati et al., 2018). Detailed micro-models use these interface elements in a refined mesh to explicitly account for the discontinuities in the material, often used to model unreinforced masonry (URM) structures that consist of distinct blocks and mortar. However, this increased level of detail comes at a high computational cost due to the need for a refined mesh (Lourenço, 1996).

The Discrete Element Method (DEM) is a family of modeling techniques that intrinsically accounts for the possible discontinuous nature of the structural problem. In the DEM, the model consists of an assembly of rigid units that are in contact through deformable interfaces. While this method allows for an accurate representation of material discontinuities, it requires a time-stepping algorithm even for solving static or buckling problems, which results in a high computational cost, as well as the need for building accurate numerical models. Different DEM formulations have been presented, among which the Distinct Element Method, initially developed in the field of rock mechanics (Cundall, 1971), and later extended to the modelling of structural components, like masonry and reinforced concrete structures (Lemos, 2007, 2019; Sarhosis et al., 2016; Scattarreggia et al., 2022; Baraldi et al., 2016). The method is nowadays implemented in the commercial software packages UDEC (Itasca, 2022) and 3DEC (Itasca, 2023). Another DEM formulation is the Non-Smooth Contact Dynamics Method (Jean, 1995, 1999), initially used for modeling granular flows using only spherical rigid elements, and next extended to 2D and 3D structural configurations, particularly to the modelling of masonry structures (Chetouane et al., 2005; Dubois et al., 2018; Taforel, 2012). The formulation has been implemented in the opensource DEM tool LMGC90 (UMontpellier, 2023). The performances of UDEC and LMGC90 were compared by the authors against different URM benchmark problems, such as pushover analyses and time-history analyses (Bouckaert et al., 2021, 2022). Some advanced models in which the discrete units are modeled with FEM and the interactions between the units are modeled with DEM have been proposed in the literature to account for deformability of the units. Those models are referred to as FEM/DEM models (Baraldi et al., 2016; Smoljanović et al.,

2018; Pulatsu et al., 2020). However, the CPU time associated to these models makes it difficult to model large structures.

An alternative approach for modeling discontinuities in structures that shares similarities with the DEM but is better suited for handling the analysis of large structures in static or dynamic problems is to treat the problem as an assembly of rigid units interconnected by deformable interfaces modeled as distributed nonlinear multidirectional springs (Malomo et al., 2018), which can represent material properties, physical discontinuities at the interfaces between units, or potential cracks in the structure (Meguro and Tagel-Din, 2000; Scattarreggia et al., 2022; Malomo et al., 2020). Various formulations that fall under this description have been proposed in the literature, such as the Rigid Block model (Portioli et al., 2015; Portioli, 2020; Orduña, 2017), the Rigid-Body Spring Model (Casolo and Uva, 2013) or the Applied Element Method (AEM) (Meguro and Tagel-Din, 1999), which is implemented in the commercial software Extreme Loading for Structures (Applied Science International, 2022). These methods are particularly interesting because the complete collapse of the structure can be simulated with a limited number of degrees of freedom (DoFs) at the structural level (Tagel-Din and Meguro, 2000, 1999). Another formulation, called the Fiber Contact Element Method (FCEM), was introduced a few years ago and brings the advantage of including multiple nonlinear springs in series at the interface, allowing for the consideration of relative deformations between blocks made of different materials (Estêvão and Oliveira, 2015; Estêvão and Carreira, 2015).

In the field of structural and soil mechanics, macro-elements have become a popular technique to capture specific phenomena, including discontinuities, with a reduced computational cost. These models use a single element to represent the behavior of large portions of the structure. This concept was first introduced for modeling soil-structure interactions (Pecker et al., 2010), and has been since then developed for many other applications including discontinuities such as the rocking of structural elements (Avgenakis and Psycharis, 2020, 2019) or for modeling URM structures (Addessi et al., 2014). Equivalent-frame models are a widely-used example of such macro-elements (Penna et al., 2014; Lagomarsino et al., 2013). Although these approaches offer reduced computational cost, they also come with

4

a loss in detail and the formulation of such elements can become extremely complex when accounting for many different phenomena.

This research paper introduces a novel approach that can handle discontinuities in structures, called the Hybrid Discrete-Finite Element Method (HybriDFEM). This new method extends the capabilities of the already existing FCEM method by including nonlinear geometric effects and nonlinear material models. A HybriDFEM model consists of a collection of rigid interacting rectangular blocks, making it well-suited for modeling discontinuities within or between structural elements. It shares similarities with the DEM method in its ability to model rigid units through contact interfaces, and with the AEM and FCEM methods in that it models contact by means of springs distributed along the units' interfaces. Despite the discontinous nature of this approach, it demonstrates a high level of precision in approximating the behavior of continuous structures, as it will be shown. One prominent feature of the HybriDFEM method is that its formulation recalls explicitly that of the FEM method (de Borst et al., 2012), making it possible to develop coupled models where parts of the structure are modeled using FEM and others with HybriDFEM. In the present contribution, it is tailored for one-directional beam-like member and its use is demonstrated for the static and buckling analysis of discontinuous structures.

Section 2 describes the implementation of the HybriDFEM method, introducing kinematic and static variables, as well as governing equations. The focus is on nonlinear geometric and material effects and the nonlinear solution procedures used to solve static problems. Section 3 demonstrates the efficacy of the HybriDFEM method through benchmarks of increasing complexity. The linear elastic analysis of beams is initially evoked. Examples of beams made of nonlinear hardening/softening materials are then provided. Next, the buckling analysis of slender and stocky columns and rigid-block assemblies is addressed by examples displaying the effect of the size of the blocks on the resulting critical load. The rocking of a column under P-Δ effects on a rigid foundation is also addressed, showcasing the potential of the present method to capture complex interface boundary conditions. Finally, a hybrid model combining rigid blocks and classical Timoshenko beam elements is presented as an example, which works as a proof of concept for the possibility to couple

5

HybriDFEM with classical FEM. This research paper offers new possibilities for analyzing structures with discontinuities, improving efficiency and accuracy.

2. HybriDFEM modelling of beam-like members

2.1. Block discretisation

In the current state of development of the HybriDFEM method, a planar structure is divided into a set of n_b rigid blocks along its longitudinal axis. This block discretization defines the total number of DoFs at the global level, similarly to what is done in AEM (Meguro and Tagel-Din, 1999). All blocks have the same dimensions except the two extremity blocks, which are truncated at half length to make their reference origin coincide with the extremities of the beam axis (Figure 1). The kinematics of each block is described by 3 degrees of freedom (DoFs), two displacements and one rotation, attached to its reference origin, which corresponds to its center of mass. This results in a system of $3n_b$ DoFs for the member, expressed in the global reference system (X, Y, Z) and collected in the vector $\mathbf{U} \in \mathbb{R}^{3n_b}$. The nodal kinematics of the generic block i are U_{3i-2}, U_{3i-1} and U_{3i} (Figure 1).

The prescribed block discretisation results in a set of $n_{CF} = n_b - 1$ contact faces (CF) between pairs of adjacent blocks. When modeling two-dimensional structures, the contact faces between blocks are, in fact, contact lines. However, the term 'contact face', which is generally chosen to indicate the interface between two blocks (Itasca, 2022), anticipates the extension of the HybriDFEM method to 3D. Since the blocks are rigid, the deformation occurs only at the CF. Each CF is characterised by 6 DoFs, corresponding to the 3 DoFs of the two contiguous blocks, which are collected into the vector $\mathbf{q}_f^{glob} \in \mathbb{R}^6$ (where the index "f" stands for "contact face"), expressed in the global reference system (X, Y, Z). The components $q_{f1}^{glob}, ..., q_{f3}^{glob}$ and $q_{f4}^{glob}, ..., q_{f6}^{glob}$ represent the kinematics of the first and second block expressed at their reference origins and will be referred to as $\mathbf{q}_{fA}^{glob}$ and $\mathbf{q}_{fB}^{glob}$, respectively.

The localisation matrix $\mathbf{A}_f \in \mathbb{R}^{6 \times 3n_b}$ relates the DoFs of the blocks to those of the CF. All the entries of this matrix are equal to 0 except at indexes where a DoF of the structure corresponds to a DoF of the CF, where the entry is equal to 1:
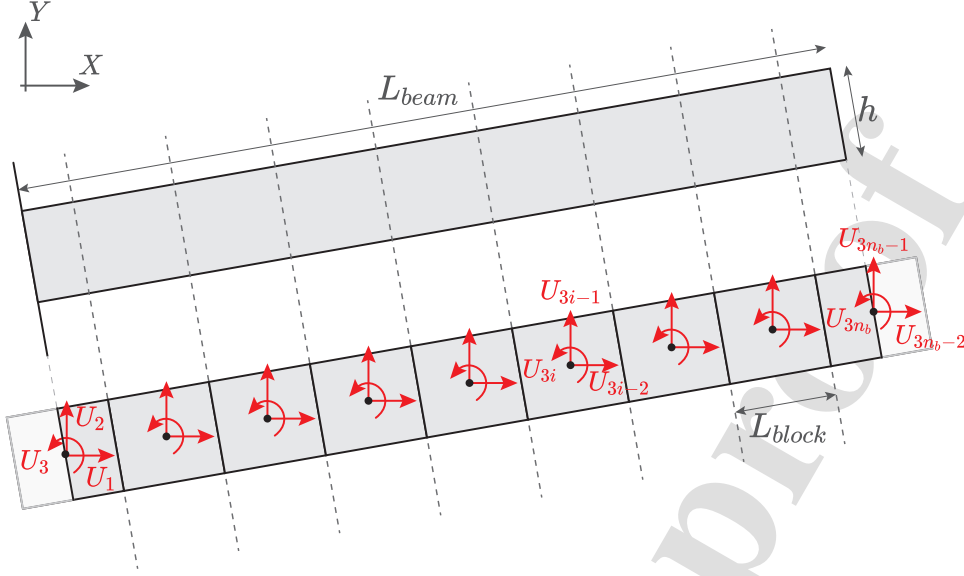
6

Figure 1: Discretisation of a cantilever beam in n_b blocks.

$$\mathbf{q}_{\mathrm{f}}^{glob} = \mathbf{A}_{\mathrm{f}}\mathbf{U}. \tag{1}$$

Computationally, this operation is identical to what is classically performed in the FEM method via incidence matrices (de Borst et al., 2012).

In the examples undertaken in this study (Section 3), the block discretisation generates a series of identical blocks, all aligned with each other. In this case, the local reference system of the blocks, oriented along the block's principal directions, is identical for all blocks, with interfaces that are perpendicular to the axis of the beam-like element (Figure 1). However, in the perspective of future developments of the presented method, the derivations carried out in this paper are done under the assumption that two adjacent blocks can be unaligned and can have different dimensions, and with CFs that can take any orientation. In this case, the local reference system of the first block differs from the local reference system of the second. These distinct local reference systems are indicated as $\left(x^{loc,A}, y^{loc,A}\right)$ and $\left(x^{loc,B}, y^{loc,B}\right)$ in Figure 3.
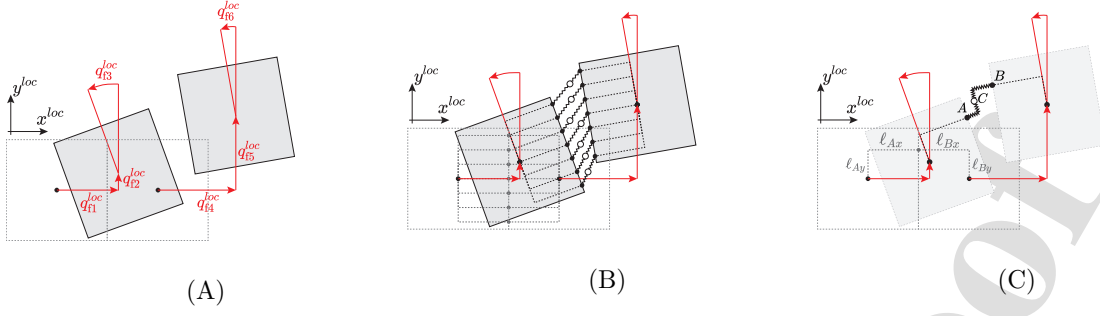
7

Figure 2: (A) Block kinematics in the local reference system (B) contact pair discretisation of the contact face (C) Isolated contact pair.

To express the nodal kinematics of the contiguous blocks in their local reference system, a transformation is performed between the global and local reference systems using the following rotation matrix:

$$\mathbf{T}(\alpha) := \begin{bmatrix} \cos\alpha & \sin\alpha & 0 \\ -\sin\alpha & \cos\alpha & 0 \\ 0 & 0 & 1 \end{bmatrix}. \tag{2}$$

The vector $\mathbf{q}_{\mathrm{f}}^{loc} \in \mathbb{R}^6$ contains the DoFs of the CF when expressed in the local reference systems of their respective blocks (Figure 2A):

$$\mathbf{q}_{\mathrm{fA}}^{loc} = \mathbf{T}(\alpha_A) \cdot \mathbf{q}_{\mathrm{fA}}^{glob} \qquad \mathbf{q}_{\mathrm{fB}}^{loc} = \mathbf{T}(\alpha_B) \cdot \mathbf{q}_{\mathrm{fB}}^{glob}, \tag{3}$$

with α_A and α_B the block orientation with respect to the global coordinate system (X, Y, Z).

2.2. Contact pair discretisation

Each CF is discretised into a series of n_c contact pairs (CPs - Figure 2B). A CP consists of two points A and B, coinciding and lying on the CF in the undeformed configuration. They are fixed on the edge of the first and second block, respectively. A bidirectional spring connects the point A to the point C, here denoted as the contact point, which in turn is connected by another bidirectional spring to the point B (Figure 2C). The quantities ℓ_{Ax} and ℓ_{Ay} (resp. ℓ_{Bx} and ℓ_{By}) indicate the position of A (resp. B) with respect to the reference origin of the corresponding block in its local reference system $\left(x^{loc,A}, y^{loc,A}\right)$ (resp.
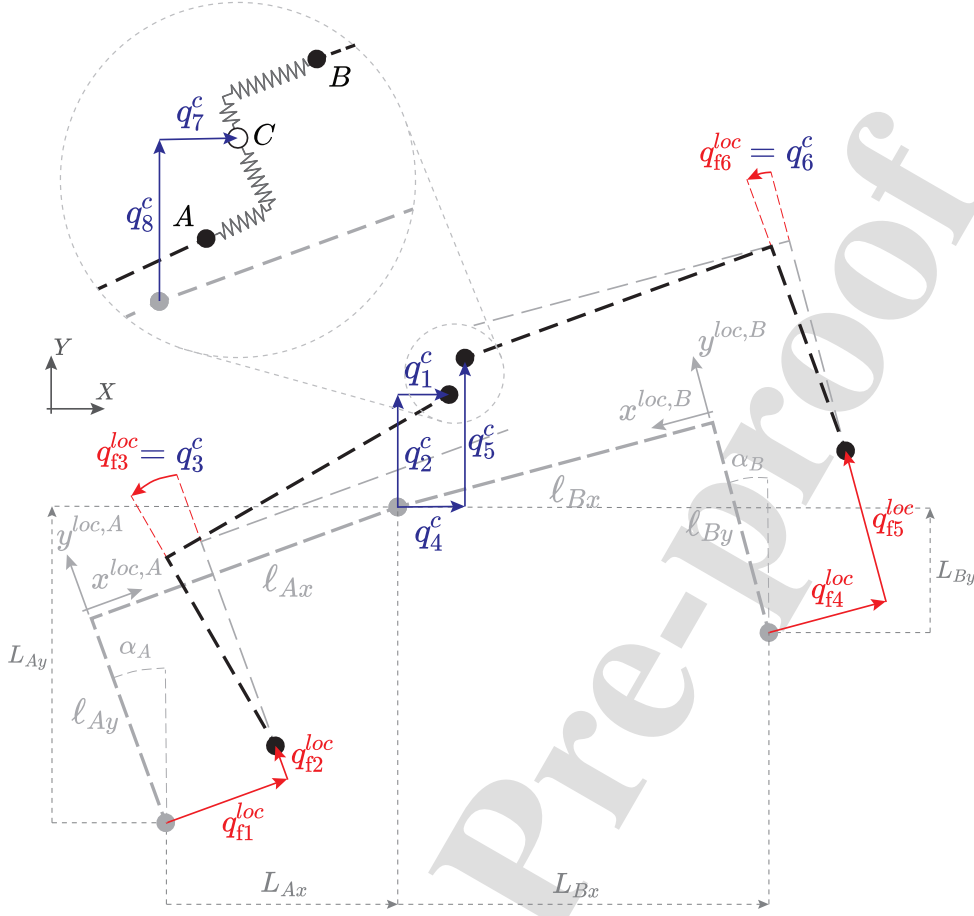
Figure 3: Local coordinates $\mathbf{q}_f^{loc}$ of a contact face and coordinates $\mathbf{q}_c$ of one of its contact pairs. N.B. the local reference system $\left(x^{loc,A}, y^{loc,A}\right)$ is in general not aligned with the local reference system $\left(x^{loc,B}, y^{loc,B}\right)$.

$\left(x^{loc,B}, y^{loc,B}\right)$). The direction of the axis $x^{loc,A}$ (resp. $x^{loc,B}$) is considered as positive from the first block's (resp. second block's) centroid to point A (resp. B), therefore ℓ_{Ax} and ℓ_{Bx} are positive quantities, whereas ℓ_{Ay} and ℓ_{By} can be positive or negative. Since the blocks are rigid and points A and B are fixed along their respective block's edge, ℓ_{Ax}, ℓ_{Bx}, ℓ_{Ay} and ℓ_{By} are constant.

2.3. Contact pair kinematics

Each CP is described by 8 DoFs: the first three are attached to point A, the next three to B and the last two to C. Said DoFs are expressed in the global reference system and stored in the vector $\mathbf{q}^c \in \mathbb{R}^8$ (Figure 3), which is subdivided into three sub-vectors $\mathbf{q}_A^c \in \mathbb{R}^3$,

9

$\mathbf{q}_B^c \in \mathbb{R}^3$, and $\mathbf{q}_C^c \in \mathbb{R}^2$, containing the kinematics of point A, B and C respectively. The last two terms $\mathbf{q}_C^c$ will be condensed for the computations at the structural level. They capture the relative elongations of the spring connected to A with respect to the spring connected to B, which offers, for example, the possibility to determine the sectional deformation profile at the interface between two blocks made of different materials (Figure 2B).

The kinematics of point A $\mathbf{q}_A^c$ depend non-linearly on the nodal kinematics of the first block (Figure 3):

$$\mathbf{q}_A^c = \begin{bmatrix} q_{\text{f1}}^{loc} \cos\alpha_A - q_{\text{f2}}^{loc} \sin\alpha_A - L_{Ay}\sin q_{\text{f3}}^{loc} - L_{Ax}\left(1 - \cos q_{\text{f3}}^{loc}\right) \\ q_{\text{f1}}^{loc} \sin\alpha_A + q_{\text{f2}}^{loc} \cos\alpha_A + L_{Ax}\sin q_{\text{f3}}^{loc} - L_{Ay}\left(1 - \cos q_{\text{f3}}^{loc}\right) \\ q_{\text{f3}}^{loc} \end{bmatrix}. \tag{4}$$

Similarly, the kinematics $\mathbf{q}_B^c$ depend on those of the second block (Figure 3):

$$\mathbf{q}_B^c = \begin{bmatrix} q_{\text{f4}}^{loc} \cos\alpha_B - q_{\text{f5}}^{loc} \sin\alpha_B - L_{By}\sin q_{\text{f6}}^{loc} + L_{Bx}\left(1 - \cos q_{\text{f6}}^{loc}\right) \\ q_{\text{f4}}^{loc} \sin\alpha_B + q_{\text{f5}}^{loc} \cos\alpha_B - L_{Bx}\sin q_{\text{f6}}^{loc} - L_{By}\left(1 - \cos q_{\text{f6}}^{loc}\right) \\ q_{\text{f6}}^{loc} \end{bmatrix}, \tag{5}$$

where, as represented in Figure 3:

$$L_{Ax} = \ell_{Ax}\cos\alpha_A - \ell_{Ay}\sin\alpha_A$$

$$L_{Ay} = \ell_{Ax}\sin\alpha_A + \ell_{Ay}\cos\alpha_A$$

$$L_{Bx} = \ell_{Bx}\cos\alpha_B + \ell_{By}\sin\alpha_B$$

$$L_{By} = -\ell_{Bx}\sin\alpha_B + \ell_{Ax}\cos\alpha_B.$$

However, it is not possible to derive $\mathbf{q}_C^c$ solely through compatibility relations, because the relative elongations of the two springs in series depend on the spring nonlinear constitutive relations. To derive the relative spring elongations, the total deformation of the CP in both directions is required, along with the orientation of the two springs in the deformed configuration. At this point, it is convenient to introduce the concept of basic displacements. They correspond to the minimum amount of kinematic information required to fully
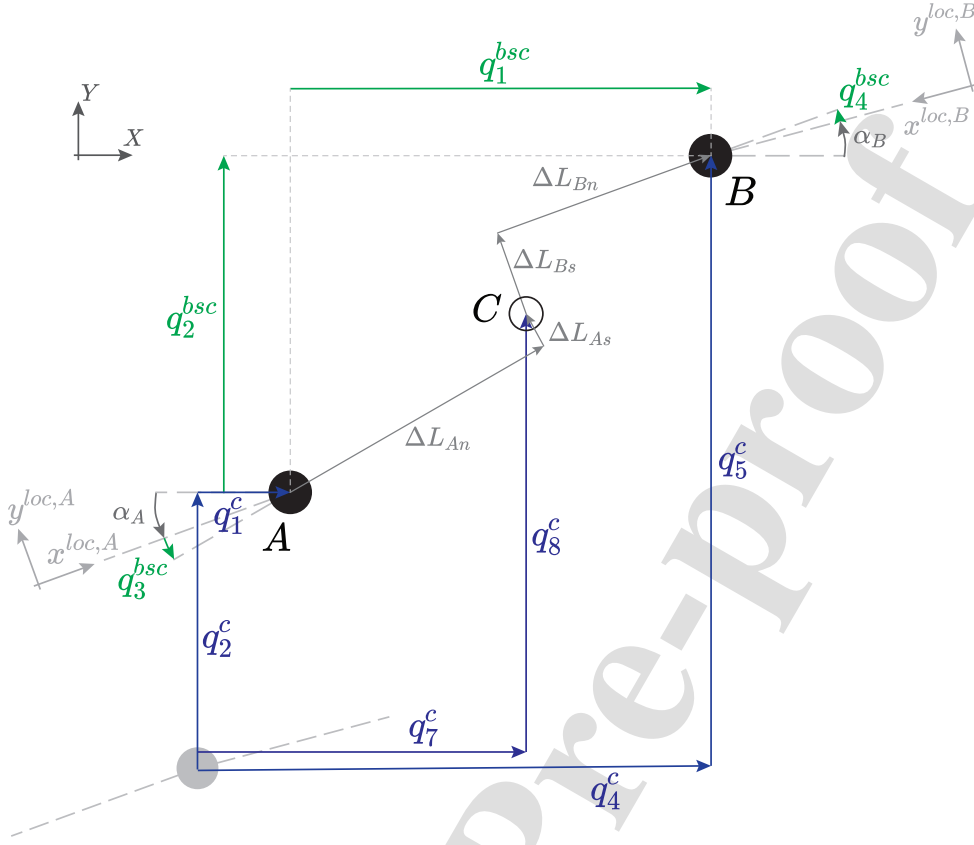
10

Figure 4: Basic displacements of the contact pair and spring elongations. Points A, B and C coincide in the undeformed configuration.

describe the deformation state of the springs, and hence they could also be called relative displacements. In other references, the terminology "natural"(Argyris et al., 1979) or "local strains"(Crisfield, 1990) shows up (where "local" is not used with the same meaning as in the current work). Herein, four basic displacements are considered: the two relative translational CP displacements along X and Y, expressed in the global reference system (X, Y, Z), and the rotations of the two springs of the CP with respect to their orientation in the undeformed configuration. They are stored in the vector $\mathbf{q}^{bsc} \in \mathbb{R}^4$ (Figure 4):

11

$$\mathbf{q}^{bsc} = \begin{bmatrix} q_4^c - q_1^c \\ q_5^c - q_2^c \\ q_3^c \\ q_6^c \end{bmatrix} \tag{6}$$

It can be argued that three basic coordinates are sufficient, instead of four, if one considers only the relative orientation of one spring with respect to the other, at the place of considering their two respective orientations with respect to the global coordinate system. This will be investigated in future works.

In the context of a nonlinear solution procedure, the incremental relation between the basic and local coordinates is needed to construct the tangent stiffness matrix of the structure, as it will become apparent later. These incremental compatibility relations are denoted $\mathbf{\Gamma} := \partial \mathbf{q}^{bsc}/\partial \mathbf{q}_{\mathrm{f}}^{loc}$ and written as:

$$\mathbf{\Gamma}\left(\mathbf{q}_{\mathrm{f}}^{loc}\right) =$$

$$\begin{bmatrix} -\cos\alpha_A & \sin\alpha_A & L_{Ay}\cos q_{\mathrm{f}3}^{loc} + L_{Ax}\sin q_{\mathrm{f}3}^{loc} & \cos\alpha_B & -\sin\alpha_B & -L_{By}\cos q_{\mathrm{f}6}^{loc} + L_{Bx}\sin q_{\mathrm{f}6}^{loc} \\ -\sin\alpha_A & -\cos\alpha_A & -L_{Ax}\cos q_{\mathrm{f}3}^{loc} + L_{Ay}\sin q_{\mathrm{f}3}^{loc} & \sin\alpha_B & \cos\alpha_B & -L_{Bx}\cos q_{\mathrm{f}6}^{loc} - L_{By}\sin q_{\mathrm{f}6}^{loc} \\ 0 & 0 & 1 & 0 & 0 & 0 \\ 0 & 0 & 0 & 0 & 0 & 1 \end{bmatrix}.$$

$$\tag{7}$$

Particular case: linear geometry

The compatibility relations expressed in Equations 4 and 5 are valid even when the blocks undergo arbitrarily large displacements. When considering small nodal displacements, one can keep just the constant and linear terms of the Taylor series expansion of those equations. In that case, the basic displacements $\mathbf{q}^{bsc}$ depend linearly on the displacements of the CF and Equation 6 (together with equations 4 and 5) is replaced by the following one:

12

$$\mathbf{q}^{bsc} = \mathbf{\Gamma}^{\text{lin}} \cdot \mathbf{q}_{\text{f}}^{loc} = \begin{bmatrix} -\cos\alpha_A & \sin\alpha_A & L_{Ay} & \cos\alpha_B & -\sin\alpha_B & -L_{By} \\ -\sin\alpha_A & -\cos\alpha_A & -L_{Ax} & \sin\alpha_B & \cos\alpha_B & -L^{Bx} \\ 0 & 0 & 1 & 0 & 0 & 0 \\ 0 & 0 & 0 & 0 & 0 & 1 \end{bmatrix} \cdot \mathbf{q}_{\text{f}}^{loc}. \tag{8}$$

It is noted that $\mathbf{\Gamma}^{\text{lin}}$ depends just on geometric properties of the undeformed configuration. In other words, the linearized compatibility relations shown in Equation 8 correspond to the computation of $\mathbf{q}^c$ and $\mathbf{q}^{bsc}$ in the undeformed configuration.

2.4. Contact model

The spring elongations, spring forces, and constitutive relations of each bidirectional spring are expressed in a reference system aligned with the orientation of the springs. The normal (or axial) direction refers to the direction perpendicular to the block's edge, denoted by the index "n", whereas the tangential (or shear) direction is parallel to the block's edge and denoted by the index "s". In particular, the above means that in the undeformed configuration, the normal direction of the spring attached to A (resp. B) is aligned with the direction of $x^{loc,A}$ (resp. $x^{loc,B}$).

The relative deformations ΔL_{An}, ΔL_{As}, ΔL_{Bn} and ΔL_{Bs} of the springs fixed to A and B, shown in Figure 4, can be computed if q_7^c and q_8^c are known, and the spring forces can be obtained from spring elongations through constitutive relations. However, $\mathbf{q}_C^c$ cannot be computed solely by means of compatibility relations as was done for $\mathbf{q}_A^c$ and $\mathbf{q}_B^c$ in equations 4 and 5. The calculation of the relative spring elongations (and consequently the displacements at the two last DoFs of the CP) must be simultaneously based on compatibility, constitutive, and equilibrium conditions.

2.4.1. Compatibility relations

The compatibility equation states that the sum of the elongations of the springs should be equal to the total basic translational deformations of the CP. Expressed in (X, Y, Z), this

condition results in the set of linear equations:

$$\mathbf{T}_2(\alpha_A + q_3^{bsc}) \cdot \begin{bmatrix} \Delta L_{An} \\ \Delta L_{As} \end{bmatrix} + \mathbf{T}_2(\alpha_B + q_4^{bsc}) \cdot \begin{bmatrix} \Delta L_{Bn} \\ \Delta L_{Bs} \end{bmatrix} = \begin{bmatrix} q_1^{bsc} \\ q_2^{bsc} \end{bmatrix}, \qquad (9)$$

with $\mathbf{T}_2(\alpha) := \begin{bmatrix} \cos\alpha & -\sin\alpha \\ \sin\alpha & \cos\alpha \end{bmatrix}.$

2.4.2. Constitutive relations

The springs characterizing each CP can be used either to represent a contact law between adjacent blocks, or an equivalent material model for the blocks. In the latter case, scaling laws must be used.

If a discontinuous structure is simulated, such as a rigid block assembly, springs are used to model the behavior at the interface between two rigid blocks, by assigning a contact law relating the spring forces $\mathbf{F}_{\text{spring}} = [F_n \quad F_s]^T$ to the spring elongations $\boldsymbol{\Delta}L = [\Delta L_n \quad \Delta L_s]^T$.

If, instead, one wishes to model a beam made of a continuous material, point A (resp. B) is assigned a representative portion of the corresponding block, of dimensions $\ell_{Ax} \times h/n_c \times b$ (resp. $\ell_{Bx} \times h/n_c \times b$), where as discussed ℓ_{Ax} corresponds to the half-length of the block, h/n_c is the total height of the section divided by the number of contact pairs, and b is the width of the section. The springs fixed to A and B are used to represent the mechanical properties of this portion of block. In other words, the entire deformation of the two block portions on each side of the CP is simulated by a concentrated deformation of the CP. A scaling law is defined, asymptotically relating the discrete and the equivalent continuous structure. The axial and shear strains ε and γ can be derived using the spring elongations (identical for B):

$$\varepsilon_A = \frac{\Delta L_{An}}{\ell_{Ax}} \qquad \text{and} \qquad \gamma_A = \frac{\Delta L_{As}}{\ell_{Ax}}, \qquad (10)$$

and from the axial and shear strains, the axial and shear stresses $\sigma(\varepsilon, \gamma)$ and $\tau(\varepsilon, \gamma)$ can be derived through constitutive relations of the material model. The normal and tangential spring forces F_n and F_s can be derived from the axial and shear stresses over the contact surface area $S := h/n_c \times b$:

$$F_n = \sigma(\varepsilon, \gamma) \cdot S \qquad \text{and} \qquad F_s = \tau(\varepsilon, \gamma) \cdot S \qquad (11)$$
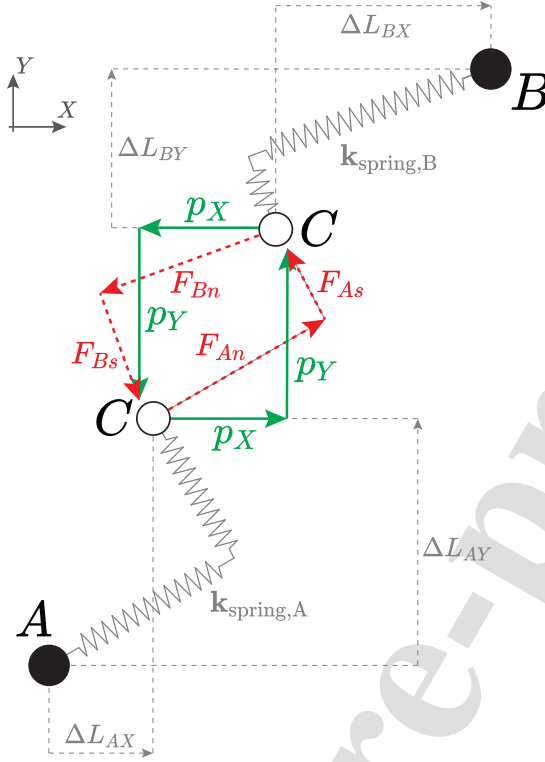
14

Figure 5: Equilibrium of forces at the contact point C.

.

In the context of a nonlinear solution procedure, the incremental relation between the spring forces and spring elongations is needed. This relation corresponds to the tangent stiffness matrix of each pair of normal+tangential springs:

$$\mathbf{k}_{\text{spring}} := \frac{\partial \mathbf{F}_{\text{spring}}}{\partial \mathbf{\Delta} L} = \begin{bmatrix} \frac{\partial F_n}{\partial \Delta L_n} & \frac{\partial F_n}{\partial \Delta L_s} \\ \frac{\partial F_s}{\partial \Delta L_n} & \frac{\partial F_s}{\partial \Delta L_s} \end{bmatrix} = \begin{bmatrix} k_{nn} & k_{ns} \\ k_{sn} & k_{ss} \end{bmatrix} \tag{12}$$

where the parameters k_{nn} and k_{ss} represent the tangent normal and tangential behaviour of the spring, and k_{ns} and k_{sn} reflect a coupling of axial and shear behaviour (dilatancy effects). In general, these parameters vary depending on the spring elongations. When modeling a continuous material, they depend on the tangent moduli of the stress-strain relation assigned to the material. This abstraction will be used in section 3 to demonstrate the ability of the method to simulate continuous materials.

15

Particular case: linear springs

If a linear spring behaviour (both for A and B) is considered, the matrix $\mathbf{k}_{\text{spring}} \in \mathbb{R}^{2\times 2}$ relates the normal and tangential deformations ΔL_n and ΔL_s with the corresponding forces F_n and F_s:

$$\mathbf{k}_{\text{spring}}\mathbf{\Delta}L = \begin{bmatrix} k_{nn} & k_{ns} \\ k_{sn} & k_{ss} \end{bmatrix} \begin{bmatrix} \Delta L_n \\ \Delta L_s \end{bmatrix} = \mathbf{F}_{\text{spring}} := \begin{bmatrix} F_n \\ F_s \end{bmatrix}, \tag{13}$$

When the beam is modeled with a linear elastic material, the axial and shear stiffness parameters assigned to the pair of springs attached to A take the form (identical for B):

$$k_{nn,A} = \frac{ES}{\ell_{Ax}}$$
$$k_{ss,A} = \chi \frac{GS}{\ell_{Ax}}, \tag{14}$$

where S is the area of the contact surface between the two portions of block, of dimensions $h/n_c \times b$, E and $G = E/(2(1+\nu))$ are the elastic and shear moduli of the material, ν the Poisson ratio, and χ a shear correction factor, typically $(6+5\nu)/(5(1+\nu))$ for beams (Stephen, 1997).

2.4.3. Equilibrium relations

The equilibrium condition states that the forces through the springs fixed to A equal the forces through the spring fixed to B, along two perpendicular directions. To satisfy equilibrium between each set of springs connected in series, their respective spring forces $\mathbf{F}_{\text{spring,A}}$ and $\mathbf{F}_{\text{spring,B}}$ must be in equilibrium. This condition is expressed in the global reference system with the spring force components p_X and p_Y and reads (Figure 5):

$$\begin{bmatrix} p_X \\ p_Y \end{bmatrix} := \mathbf{T}_2(\alpha_A + q_3^{bsc}) \cdot \begin{bmatrix} F_{An}(\Delta L_{An}, \Delta L_{As}) \\ F_{As}(\Delta L_{An}, \Delta L_{As}) \end{bmatrix} = \mathbf{T}_2(\alpha_B + q_4^{bsc}) \cdot \begin{bmatrix} F_{Bn}(\Delta L_{Bn}, \Delta L_{Bs}) \\ F_{Bs}(\Delta L_{Bn}, \Delta L_{Bs}) \end{bmatrix}, \tag{15}$$

which expresses the equilibrium condition, directly incorporating the spring constitutive relations.

16

2.4.4. Internal nonlinear solution procedure

The combination of the compatibility relations expressed in equation 9 and the equilibrium relations in equation 15 results in a set of two linear (compatibility) and two possibly nonlinear (equilibrium) equations expressed in terms of four unknowns ΔL_{An}, ΔL_{As}, ΔL_{Bn} and ΔL_{Bs}. This set of equations is solved by means of a Newton-Raphson procedure, which will be referred to as the internal nonlinear solution procedure, because it is repeated at every load step and iteration of the external nonlinear solution procedure applied at the global level. More details about the nonlinear solution procedures will be given in section 2.6.

Particular case: linear springs

When linear springs are employed, e.g. when modeling a homogenous member with a linear elastic material, the combination of the compatibility and equilibrium equations results in a set of four linear equations:

$$
\begin{bmatrix}
\mathbf{T}_2(\alpha_A + q_3^{bsc}) & \mathbf{T}_2(\alpha_B + q_4^{bsc}) \\
\mathbf{T}_2(\alpha_A + q_3^{bsc}) \cdot \mathbf{k}_{\text{spring,A}} & -\mathbf{T}_2(\alpha_B + q_4^{bsc}) \cdot \mathbf{k}_{\text{spring,B}}
\end{bmatrix}
\begin{bmatrix}
\mathbf{\Delta} L_A \\
\mathbf{\Delta} L_B
\end{bmatrix}
=
\begin{bmatrix}
q_1^{bsc} \\
q_2^{bsc} \\
0 \\
0
\end{bmatrix}.
\tag{16}
$$

Therefore, the nonlinear solution procedure at the level of the contact pair is not required.

2.5. Contact pair equilibrium

When the internal nonlinear solution procedure reaches convergence, the spring elongations $\mathbf{\Delta} L$, spring forces $\mathbf{F}_{\text{spring}}$, and $\mathbf{q}_C^c$ are obtained. Since $\mathbf{q}_C^c$ is known, the relative elongations of the springs attached to A and B, expressed in the global reference system, can be derived (Figure 5):
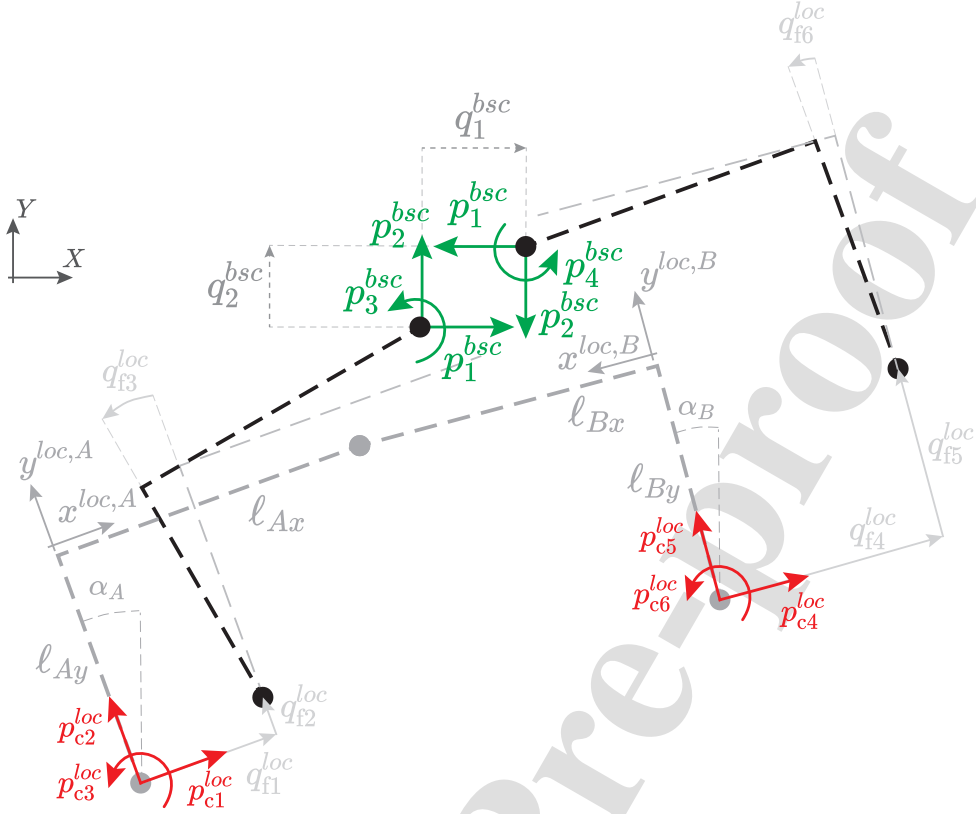
17

Figure 6: Basic forces at the contact point and local resisting forces of one CP at the center of mass of the two blocks contiguous.

$$\Delta L_{AX} = q_7^c - q_1^c$$

$$\Delta L_{AY} = q_8^c - q_2^c$$

$$\Delta L_{BX} = q_4^c - q_7^c$$

$$\Delta L_{BY} = q_5^c - q_8^c$$

The basic resisting forces $\mathbf{p}^{bsc}$ associated to the basic displacements $\mathbf{q}^{bsc}$ can be found by establishing equilibrium in the deformed configuration (Figure 6):

$$
\mathbf{p}^{bsc} = \begin{bmatrix} p_X \\ p_Y \\ p_X \cdot \Delta L_{AY} - p_Y \cdot \Delta L_{AX} \\ p_X \cdot \Delta L_{BY} - p_Y \cdot \Delta L_{BX} \end{bmatrix}, \tag{17}
$$

which corresponds to the energy conjugate of the basic displacements defined in equation 6. The two last terms of the vector of basic resisting forces $\mathbf{p}^{bsc}$, i.e. the two resisting moments at A and B respectively, account for the fact that points A, B and C are unaligned in the deformed configuration. They arise from the additional lever arm created when the CP deforms. The vector $\mathbf{p}^c$ of resisting forces of the CP, expressed at points A, B and C can be obtained from $\mathbf{p}^{bsc}$ and corresponds to the energy conjugate of $\mathbf{q}^c$:

$$
\mathbf{p}^c = \begin{bmatrix} \mathbf{p}^c_A \\ \mathbf{p}^c_B \\ \mathbf{p}^c_C \end{bmatrix} = \begin{bmatrix} -p_1^{bsc} & -p_2^{bsc} & p_3^{bsc} & p_1^{bsc} & p_2^{bsc} & p_4^{bsc} & 0 & 0 \end{bmatrix}^T, \tag{18}
$$

in which $\mathbf{p}^c_C = \mathbf{0}$, highlighting the condensation of the variables relative to point C at the structural level. The resisting forces $\mathbf{p}^{loc}_c$ of the CP expressed in the local reference systems of the two blocks composing the CF are derived directly from $\mathbf{p}^{bsc}$ by establishing equilibrium in the undeformed configuration (Figure 6):

$$
\mathbf{p}^{loc}_c = \begin{bmatrix} \mathbf{p}^{loc}_{cA} \\ \mathbf{p}^{loc}_{cB} \end{bmatrix} = \begin{bmatrix} -\cos\alpha_A & -\sin\alpha_A & 0 & 0 \\ \sin\alpha_A & -\cos\alpha_A & 0 & 0 \\ L_{Ay}\cos q^{loc}_{f3} + L_{Ax}\sin q^{loc}_{f3} & -L_{Ax}\cos q^{loc}_{f3} + L_{Ay}\sin q^{loc}_{f3} & 1 & 0 \\ \cos\alpha_B & \sin\alpha_B & 0 & 0 \\ -\sin\alpha_B & \cos\alpha_B & 0 & 0 \\ -L_{By}\cos q^{loc}_{f6} + L_{Bx}\sin q^{loc}_{f6} & -L_{Bx}\cos q^{loc}_{f6} - L_{By}\sin q^{loc}_{f6} & 0 & 1 \end{bmatrix} \cdot \mathbf{p}^{bsc}, \tag{19}
$$

which is coherent with the principle of contragradiency in structural analysis, since from equations 7 and 19, $\mathbf{p}^{loc}_c = \mathbf{\Gamma}(\mathbf{q}^{loc}_f)^T \cdot \mathbf{p}^{bsc}$. The energy conjugate of the vector $\mathbf{p}^{loc}_c$ is a

19

vector $\mathbf{q}_c^{loc}$ describing the CP kinematics from the perspective of the two block's centroids. However, this vector is trivial, since it is equal to $\mathbf{q}_f^{loc}$ for all the CPs on one CF.

Particular case: linear geometry

When nonlinear geometric effects are neglected, equilibrium is established in the undeformed configuration, and equation 19 simplifies to:

$$\mathbf{p}_c^{loc} = \left(\mathbf{\Gamma}^{\mathrm{lin}}\right)^T \cdot \mathbf{p}^{bsc} \tag{20}$$

The resisting actions of one contact face expressed in its local reference system is the sum of the contributions of each CP composing the CF:

$$\mathbf{p}_f^{loc} = \begin{bmatrix} \mathbf{p}_{fA}^{loc} \\ \mathbf{p}_{fB}^{loc} \end{bmatrix} = \sum_{c \in \mathrm{CF}} \mathbf{p}_c^{loc}. \tag{21}$$

The CF resisting forces expressed in the global reference system depend on the orientation of the two blocks contiguous to the CF in its undeformed configuration with respect to the horizontal:

$$\mathbf{p}_{fA}^{glob} = \mathbf{T}(\alpha_A)^T \cdot \mathbf{p}_{fA}^{loc} \qquad \mathbf{p}_{fB}^{glob} = \mathbf{T}(\alpha_B)^T \cdot \mathbf{p}_{fB}^{loc} \tag{22}$$

By assembling the resisting forces of all the contact faces via the incidence matrices (see equation 1), one obtains:

$$\mathbf{P}_r = \sum \mathbf{A}_f^T \mathbf{p}_f^{glob}, \tag{23}$$

the resisting forces $\mathbf{P}_r$ of the structure at the global level can be computed. This vector is the energy conjugate of the vector of global displacements $\mathbf{U}$ of the structure, and contains the resisting forces of the structure expressed as forces and moments at the centroid of each block.

2.6. External nonlinear solution procedure

The derivations presented in the previous sections give a step-by-step procedure to compute the global resisting forces $\mathbf{P}_r$ of the structure from a given set of nodal kinematics
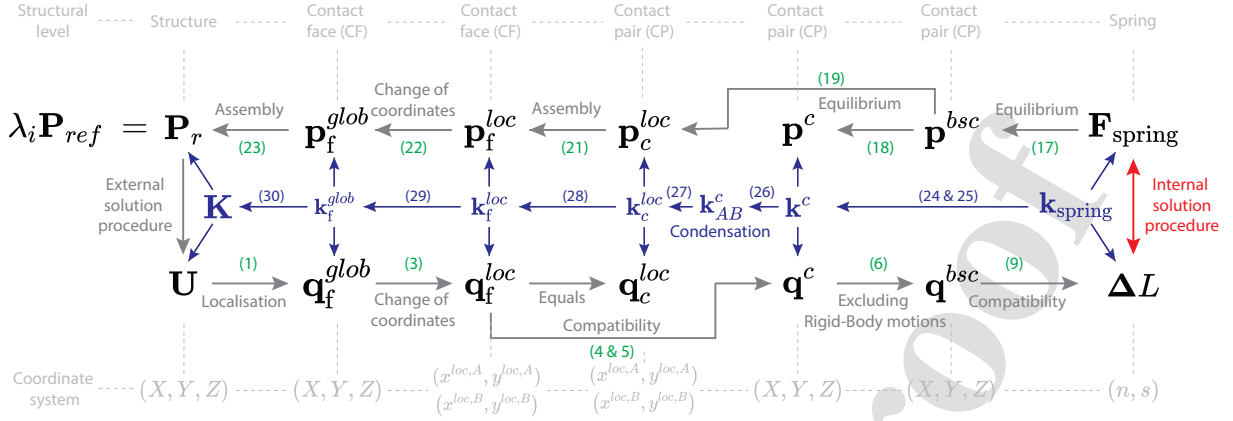
Figure 7: Graphical roadmap for the computation of the static and kinematic quantities of HybriDFEM, with identification of the corresponding stiffness matrices as well as of the external and internal nonlinear solution procedures.

$\mathbf{U}$. The kinematic variables of the structure, the contact faces, the contact pairs and the springs composing the contact pairs are derived through compatibility equations, and their corresponding static counterparts (energy conjugates) are derived through equilibrium equations. They could have been alternatively derived by the Principle of Virtual Work. The full procedure is summarized in Figure 7. When nonlinear effects are included, this relation is not invertible and an iterative nonlinear solution procedure is required to find, at each load step or increment i, the nodal displacements $\mathbf{U}$ for which the resisting forces are in equilibrium with the external forces $\lambda_i \mathbf{P}_{\text{ref}}$ applied to the structure, where $\mathbf{P}_{\text{ref}}$ is a given reference load pattern and the applied forces are incremented proportionally to $\mathbf{P}_{\text{ref}}$ by a factor λ_i. Three nonlinear solution procedures were implemented in the scope of the present study. In a classical Newton-Raphson procedure, the load increment is kept constant from one iteration to the other. In a displacement-control procedure, the value of the load increment is computed such that the nodal displacement of a controlled DoF "m", U_m, is kept constant. Finally, in a work-control procedure, the external work performed by the applied forces is kept constant. The validity of these three methods in performing nonlinear static and buckling analyses is demonstrated in what follows.

To obtain quadratic convergence of the nonlinear solution procedures, the tangent stiff-

ness matrix of the structure is computed at each iteration. This operation starts at the spring level, for which the tangent stiffness matrix $\mathbf{k}_{\text{spring}}$ is shown in equation 12, expressed with respect to (n, s), the normal and tangential axis of the spring. For the springs attached to points A and B, this stiffness matrix can be expressed in the global coordinate system (X, Y, Z). For the spring attached to A, it yields (similar for B):

$$\mathbf{k}_{A,XY} := \begin{bmatrix} k_{A,XX} & k_{A,XY} \\ k_{A,XY} & k_{A,YY} \end{bmatrix} = \mathbf{T}_2 \left(\alpha_A + q_3^{bsc} \right) \cdot \mathbf{k}_{\text{spring,A}} \cdot \mathbf{T}_2^T \left(\alpha_A + q_3^{bsc} \right). \tag{24}$$

From the expressions of the stiffness matrices of the two springs expressed in the global coordinate system, the stiffness matrix of the contact pair, $\mathbf{k}^c = \partial \mathbf{p}^c / \partial \mathbf{q^c}$ can be derived:

$$\mathbf{k}^c = \begin{bmatrix} \mathbf{k}_{AA}^c & \mathbf{0} & \mathbf{k}_{AC}^c \\ 0 & \mathbf{k}_{BB}^c & \mathbf{k}_{BC}^c \\ \mathbf{k}_{AC}^c{}^T & \mathbf{k}_{BC}^c{}^T & \mathbf{k}_{CC}^c \end{bmatrix}$$

$$= \begin{bmatrix} k_{A,XX} & k_{A,XY} & k_{13} & 0 & 0 & 0 & -k_{A,XX} & -k_{A,XY} \\ k_{A,XY} & k_{A,YY} & k_{23} & 0 & 0 & 0 & -k_{A,XY} & -k_{A,YY} \\ k_{13} & k_{23} & k_{33} & 0 & 0 & 0 & -k_{13} & -k_{23} \\ 0 & 0 & 0 & k_{B,XX} & k_{B,XY} & k_{46} & -k_{B,XX} & -k_{B,XY} \\ 0 & 0 & 0 & k_{B,XY} & k_{B,YY} & k_{56} & -k_{B,XY} & -k_{B,YY} \\ 0 & 0 & 0 & k_{46} & k_{56} & k_{66} & -k_{46} & -k_{56} \\ -k_{A,XX} & -k_{A,XY} & -k_{13} & -k_{B,XX} & -k_{B,XY} & -k_{46} & k_{77} & k_{78} \\ -k_{A,XY} & -k_{A,YY} & -k_{23} & -k_{B,XY} & -k_{B,YY} & -k_{56} & k_{78} & k_{88} \end{bmatrix}, \tag{25}$$

with:

$$k_{13} = k_{A,XY} \Delta L_{AX} - k_{A,XX} \Delta L_{AY}$$

$$k_{23} = k_{A,YY} \Delta L_{AX} - k_{A,XY} \Delta L_{AY}$$

$$k_{33} = k_{A,YY} \Delta L_{AX}^2 + k_{A,XX} \Delta L_{AY}^2 - 2k_{A,XY} \Delta L_{AY} \Delta L_{AX}$$

$$k_{46} = k_{B,XX} \Delta L_{BY} - k_{B,XY} \Delta L_{BX}$$

$$k_{56} = k_{B,XY} \Delta L_{AY} - k_{B,XY} \Delta L_{BX}$$

$$k_{66} = k_{B,YY} \Delta L_{BX}^2 + k_{B,XX} \Delta L_{BY}^2 - 2k_{B,XY} \Delta L_{BY} \Delta L_{BX}$$

22

$$k_{77} = k_{A,XX} + k_{B,XX}$$

$$k_{78} = k_{A,XY} + k_{B,XY}$$

$$k_{88} = k_{A,YY} + k_{B,YY}$$

The stiffness matrix of the contact pair is then condensed to express the incremental relation between the kinematic and static variables of points A and B only, through $\mathbf{k}_{AB}^c :=$ $\partial \mathbf{p}_{AB}^c / \partial \mathbf{q}_{AB}^c$, with $(\mathbf{p}_{AB}^c)^T = \left[(\mathbf{p}_A^c)^T \ (\mathbf{p}_B^c)^T \right]$ (similar for $\mathbf{q}_{AB}^c$):

$$\mathbf{k}_{AB}^c = \begin{bmatrix} \mathbf{k}_{AC}^c & \mathbf{0} \\ \mathbf{0} & \mathbf{k}_{BC}^c \end{bmatrix} - \begin{bmatrix} \mathbf{k}_{AC}^c \\ \mathbf{k}_{BC}^c \end{bmatrix} \cdot \mathbf{k}_{CC}^c \cdot \left[(\mathbf{k}_{AC}^c)^T \ (\mathbf{k}_{BC}^c)^T \right] \tag{26}$$

This stiffness matrix can then be expressed with respect to the local coordinates of the CF by defining the incremental relation $\boldsymbol{\Gamma}_{AB}^c := \partial \mathbf{q}_{AB}^c / \partial \mathbf{q}_f^{loc}$. Similarly to equation 19, which relates $\mathbf{p}_c^{loc}$ to $\mathbf{p}^{bsc}$ through $\boldsymbol{\Gamma}\left(\mathbf{q}_f^{loc}\right)$, the matrix $\boldsymbol{\Gamma}_{AB}^c$ relates $\mathbf{p}_c^{loc}$ to $\mathbf{p}_{AB}^c$, hence $\mathbf{p}_c^{loc} = (\boldsymbol{\Gamma}_{AB}^c)^T \cdot \mathbf{p}_{AB}^c$:

$$\begin{aligned} \mathbf{k}_c^{loc} = \frac{\partial \mathbf{p}_c^{loc}}{\partial \mathbf{q}_f^{loc}} &= \frac{\partial \left((\boldsymbol{\Gamma}_{AB}^c)^T \cdot \mathbf{p}_{AB}^c \right)}{\partial \mathbf{q}_f^{loc}} \\ &= \frac{\partial \left((\boldsymbol{\Gamma}_{AB}^c)^T \right)}{\partial \mathbf{q}_f^{loc}} \cdot \mathbf{p}_{AB}^c + (\boldsymbol{\Gamma}_{AB}^c)^T \cdot \frac{\partial \mathbf{p}_{AB}^c}{\partial \mathbf{q}_{AB}^c} \cdot \frac{\partial \mathbf{q}_{AB}^c}{\partial \mathbf{q}_f^{loc}} \\ &= \frac{\partial \left((\boldsymbol{\Gamma}_{AB}^c)^T \right)}{\partial \mathbf{q}_f^{loc}} \cdot \mathbf{p}_{AB}^c + (\boldsymbol{\Gamma}_{AB}^c)^T \cdot \mathbf{k}_{AB}^c \cdot \boldsymbol{\Gamma}_{AB}^c, \end{aligned} \tag{27}$$

where the first term of this equation accounts for nonlinear geometric effects, and the second terms relates to the tangent stiffness of the contact pair in its deformed configuration. The tangent stiffness matrices of all CPs composing a CF can then be assembled to obtain the stiffness matrix of the CF expressed in its local coordinate system:

$$\mathbf{k}_f^{loc} = \begin{bmatrix} \mathbf{k}_{f,AA}^{loc} & \mathbf{k}_{f,AB}^{loc} \\ \mathbf{k}_{f,BA}^{loc} & \mathbf{k}_{f,BB}^{loc} \end{bmatrix} = \sum_{c \in \text{CF}} \mathbf{k}_c^{loc}, \tag{28}$$

23

The latter should then be expressed in the global coordinate system:

$$
\mathbf{k}_{\mathrm{f}}^{glob} = \begin{bmatrix} \mathbf{T}(\alpha_A)^T \mathbf{k}_{\mathrm{f},AA}^{loc} \mathbf{T}(\alpha_A) & \mathbf{T}(\alpha_A)^T \mathbf{k}_{\mathrm{f},AB}^{loc} \mathbf{T}(\alpha_B) \\ \mathbf{T}(\alpha_B)^T \mathbf{k}_{\mathrm{f},BA}^{loc} \mathbf{T}(\alpha_A) & \mathbf{T}(\alpha_B)^T \mathbf{k}_{\mathrm{f},BB}^{loc} \mathbf{T}(\alpha_B) \end{bmatrix}.
\tag{29}
$$

Finally, the tangent stiffness matrix of the structure expressed in the global reference system can be assembled:

$$
\mathbf{K} = \sum \mathbf{A}_{\mathrm{f}}^T \mathbf{k}_{\mathrm{f}}^{glob} \mathbf{A}_{\mathrm{f}}
\tag{30}
$$

This tangent stiffness matrix, which accounts for the nonlinear geometric and material effects, is recomputed at each iteration in the external solution procedure to achieve quadratic convergence.

3. Application examples

3.1. Linear elastic analysis of beams

The HybriDFEM method is an extension of the FCEM method, whose ability in solving linear elastic problems has already been partially demonstrated (Estêvão and Oliveira, 2015). For the sake of completeness, examples of linear elastic analysis have been implemented also in the developed HybriDFEM script.

The numerical examples consist of two 3m-long beams with a rectangular cross-section of dimension $h \times b = 0.5$ m $\times$ 0.2 m, subjected to a tip vertical downwards force of 100 kN. They are composed of a homogeneous linear elastic material with $E = 30$ GPa and $\nu = 0$. They differ with respect to the boundary conditions: the first beam (B1) is a cantilever beam, whereas the second (B2) has an additional support at mid-span (Figure 8).

The benchmark consists of two beams with different levels of discretisation, both at the block and CP level. In particular, for a given CP discretization, the number of blocks composing the beam is progressively increased and the solution computed by HybriDFEM is checked against the solution of a continuous beam element. In particular, the vertical displacement of the free end of the beam is compared with the analytical solution of a Timoshenko beam, computed with a shear correction factor of $\chi = 6/5$ (Timoshenko and
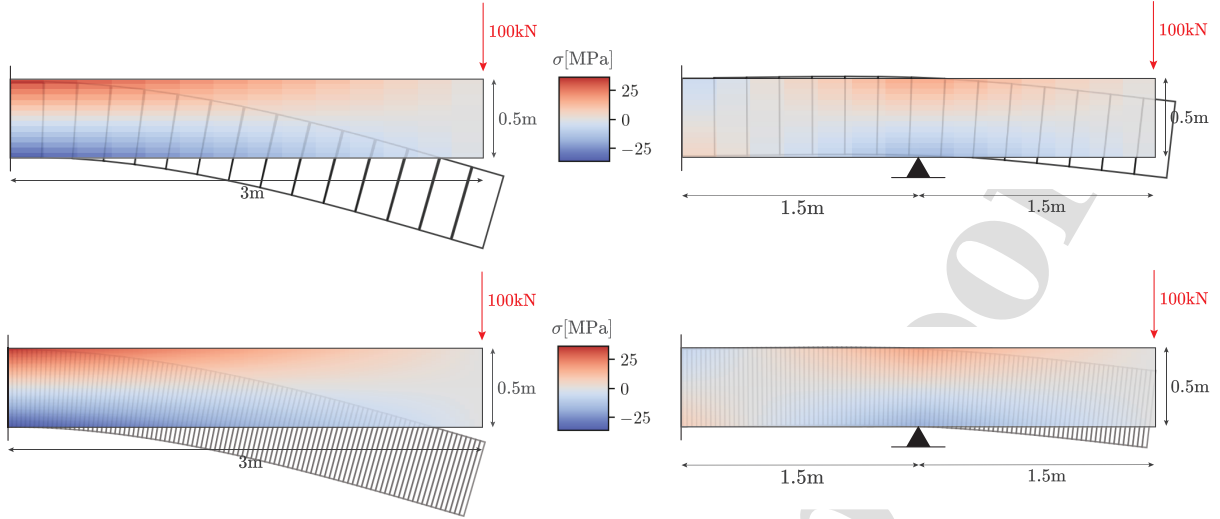
24

Figure 8: Axial stresses and deformed shape ($\times 40$) of beams B1 (left) and B2 (right) with coarse (15 blocks $\times$ 15 CPs) and fine (100 blocks $\times$ 100 CPs) discretisation.

Gere, 1961). Since the problem is linear, the displacements for which the associated resisting forces are equal to the applied forces are computed directly by inversion of the stiffness matrix of the structure. The analytical value of vertical displacement of the free end, computed using the unit dummy force theorem, is equal to $\delta_{B1} = 14.64$ mm for B1 and $\delta_{B2} = 3.54$ mm for B2, which is a statically indeterminate structure.

The results are visible in Figure 9. The percentage error, corresponding to the difference between the computed and analytical displacement, divided by the latter, reaches 0.00% for the finest discretisation of B1, with 100 blocks generating 99 CFs, each divided into 100 CPs. For B2, the percentage error is -0.48% for the same discretisation. The fact that HybriDFEM predicts smaller displacements than the analytical value for coarse block discretisation, but larger displacements for coarse CP discretisation, both for B1 and B2, suggests that a small number of blocks tends to overestimate the stiffness of the beam, whereas a small number of CPs tends to underestimate it.

The axial stresses in beams B1 and B2 are displayed in Figure 8 for a fine and coarse discretisation of 15 blocks $\times$ 15 CPs and 100 blocks $\times$ 100 CPs, respectively. The analytical value of the maximal axial stress is 36 MPa for B1 and 18 MPa for B2. For B1, the
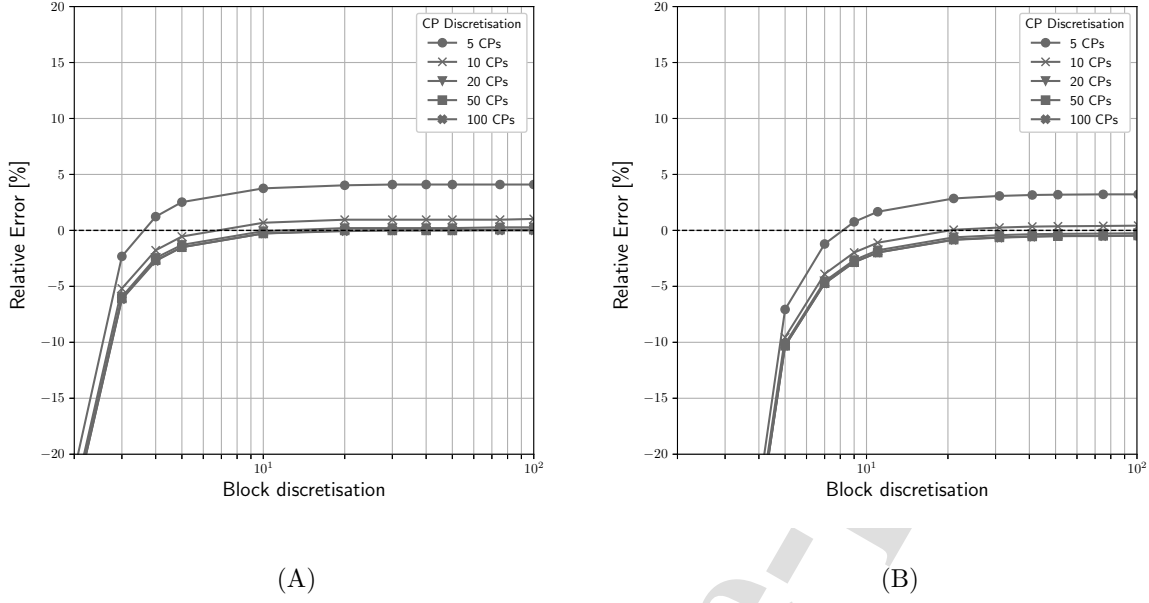
25

Figure 9: Influence of the CP and block discretisation on the beam displacement for (A) B1 and (B) B2.

maximal stress was 32.54 MPa for the coarse and 35.46 MPa for the fine discretisation, which corresponds to an error of -9.61% and -1.5%, respectively. For B2, the maximal stress was 15.67 MPa (-12.94%) for the coarse and 17.64 MPa (-2%) for the fine discretisation. It is important to note that a lower value of axial stress with respect to the analytical solution was expected since it represents an average of the axial stress over the contact surface area associated to each contact pair. Moreover, the model computes the stresses at the CFs, which does not correspond exactly to the extremity of the beam.

3.2. Beam with nonlinear material response

A nonlinear material model has been thereafter implemented in the beam B1 to investigate the capability of HybriDFEM to capture its response. The material model adopted for this example is a bilinear axial stress-strain relationship:

$$\begin{cases} \sigma = \varepsilon E_0 & \text{when} & \mid \varepsilon \mid \le \varepsilon_y \\ \sigma = f_y + \alpha(\varepsilon - \varepsilon_y)E_0 & \text{when} & \mid \varepsilon \mid > \varepsilon_y \end{cases}, \tag{31}$$

26

with $E_0 = 30$ GPa and $\nu = 0$ (similarly to section 3.1), a yield strength in tension and compression $f_y = 20$ MPa, and five values for the strain-hardening parameter α: 10%, 5%, 0%, -5% and -10%. The first two correspond to a material with hardening behaviour, the last two to a material with softening behaviour, and the third value corresponds to an elastic-perfectly plastic material. The discretisation adopted in this example is 50 blocks × 35 CPs, which has shown to be a satisfactory compromise between precision and required computational time, for linear elastic analysis.

A downwards vertical load P is applied at the free end of the beam and is controlled by means of a displacement-control procedure, increasing progressively the rotation of the second leftmost block, next to the first one being fixed in the three directions. The validation of the HybriDFEM code in this example is done by means of a sectional analysis, comparing the curvature of the beam at the leftmost CF and the associated bending moment with the analytical expression of the moment-curvature relation of a beam with rectangular cross-section and bilinear material (Pandit and Srinivasan, 2016):

$$\begin{cases} M^* = \kappa^* & \text{when} \quad \kappa^* \leq 1 \\ M^* = \frac{1}{2}\left(3 - \frac{1-\alpha}{(\kappa^*)^2}\right) + \alpha\left(\kappa^* - \frac{3}{2}\right) & \text{when} \quad \kappa^* > 1 \end{cases}, \tag{32}$$

where M^* is the moment normalized with respect to the moment at first yield $M_0 = bh^2 f_y/6$ and κ^* is the curvature normalized with respect to the curvature at first yield $\kappa_0 = (2f_y)/(E_0 h)$.

The $\kappa^* - M^*$ curves obtained by the model for the five values of α are displayed and compared to the analytical ones in Figure 10, showing very satisfactory agreement with the analytical curves. Convergence studies have been performed to assess the influence of block and CP discretisation, where the same simulation was run first with a varying block discretisation with a very fine CP discretisation (200 CPs), then with a varying CP discretisation with a very fine block discretisation (200 blocks). It has been observed that, in this sectional analysis, the block discretisation has no influence on the relative error between the numerical and analytical $\kappa^* - M^*$ curves. Since the number of interfaces is directly related to the number of blocks, the block discretisation only has an influence on
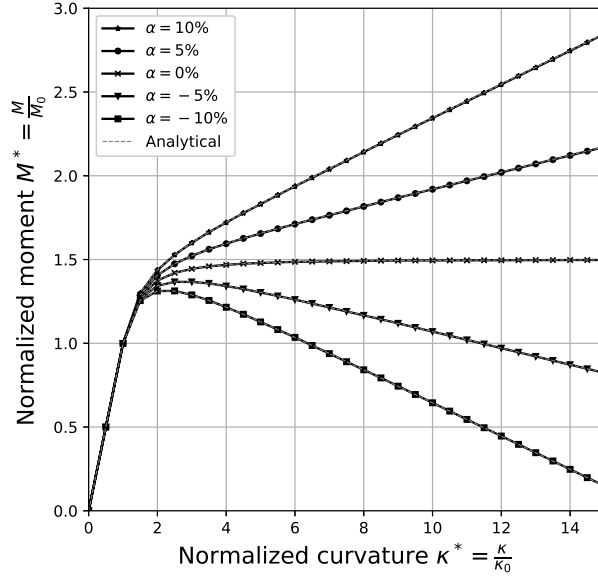
27

Figure 10: Moment-curvature relation for beam B1 with bilinear material and different values of strain-hardening ratio α.

the number of points along the beam at which the value of the curvature can be known. Figures 11 (A) and (B) show the influence of the CP discretisation for a material with hardening or softening behaviour, respectively. With 20 CPs or more, the percentage error is negligible. For the hardening material, the error computed for large values of κ^*, where nearly all the CPs have yielded, converges back to the percentage error obtained when the beam behaves linearly ($\kappa^* < 1$). For the softening material, the relative error increases for large values of κ^* and lower number of CPs.

3.3. Buckling analysis of beam-columns

The ability of the HybriDFEM method in modelling geometric nonlinearities is tested by conducting the buckling analysis of beam-columns with different boundary conditions, length-to-height ratio, and size ratio. In this benchmark, the same linear elastic material as in section 3.1 is used.

The first column that is considered is 4m high and relatively slender, with $L/h = 20$. The
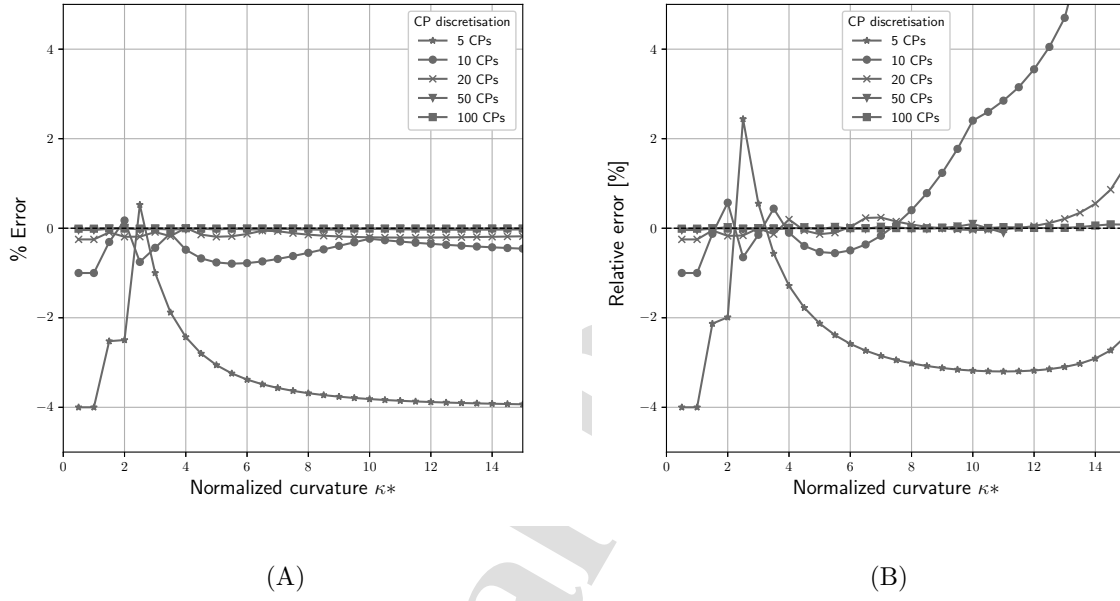
28

(A)

(B)

Figure 11: Influence of the CP discretisation on the moment-curvature relation for (A) hardening material with $\alpha = 10\%$, and (B) softening material with $\alpha = -10\%$. The block discretisation is the same for all simulations (200 blocks).

29

cross-section of the beam is squared, with $h = 0.2$ m. The adopted beam discretisation is the same as in section 3.2. Four different boundary conditions are implemented: fixed-fixed (FF), fixed-free (FFr), fixed-pinned (FP) and pinned-pinned (PP). A small perturbation is introduced in the column, by means of a constant horizontal force $F_h = 10$ N to the left, applied at mid-height of the column. The horizontal displacement of the node on which F_h is applied is denoted δ and is monitored throughout the whole simulation. Its initial value, when only F_h is applied on the column, is denoted δ_0. A monotonically increasing axial compression force F_v is then applied on the top of the column, controlled by means of a work-control procedure (de Borst et al., 2012). The vertical force applied at the last converged step is compared with the theoretical Euler buckling load $N_{cr,E} = \pi^2 EI/L_f^2$.

The graph in Figure 12 shows, for the 4 different boundary conditions considered, the increase in horizontal displacement, $\delta - \delta_0$, normalized with respect to δ_0, against the applied vertical force normalized with respect to the theoretical Euler load. The error between the maximum vertical load and the theoretical one is between -3.15% (FFr) and -1.48% (PP). The obtained buckling modes for each set of boundary conditions are also visible on Figure 12, agreeing with the expected buckling modes of a continuous beam-column.

A convergence study was conducted to evaluate the influence of the CP discretisation while varying the number of blocks. Figure 13 shows the influence of both discretisations on the relative error between the vertical load obtained at the last converged step with respect to the theoretical Euler buckling load for the pinned-pinned (PP) slender column. A coarse CP discretisation yields values of the critical load that are significantly lower than the theoretical one. From 30 blocks onwards, the relative error does not improve significantly when increasing the number of blocks. It is important to note that the maximal load obtained numerically is the load applied at the last converged equilibrium point in the simulation and therefore also depends on the number of increments chosen for the simulation, since a larger number of increments allow to get closer to the exact solution. In this case, all simulations were run in 80 increments. Finally, diminishing the relative size of the beam blocks brings to a buckling solution for the discrete system that is closer to the theoretical one for the continuous column. For a column made of 10, or more, blocks, the difference between the
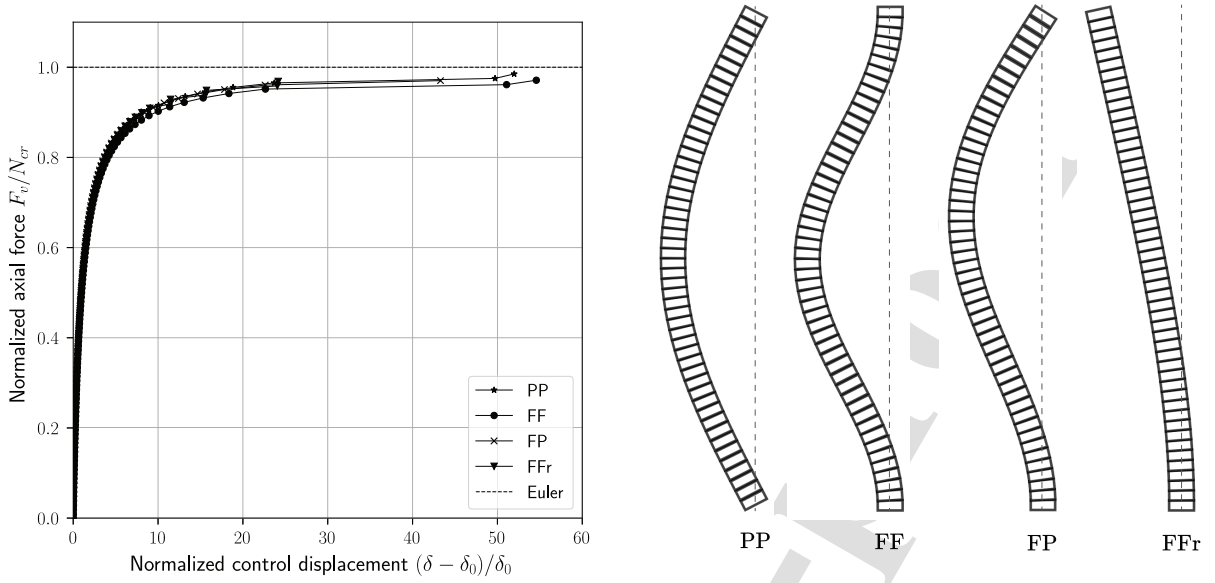
Figure 12: Buckling response of a slender column with different boundary conditions.

computed and estimated value is less than 3% for 10 CPs or more. The influence of the size of the blocks with respect to the size of the column becomes particularly visible for columns made up of 6, or less, blocks.

The benchmark was repeated for a relatively stocky column of height 4 m and $L/h = 4$. The cross-section of the beam is rectangular with $h \times b = 1$ m $\times$ 0.2 m. The adopted discretisation and boundary conditions, as well as the applied loading procedure, are the same as for the slender column. Because the column is stocky, its shear deformations become non negligible compared to flexural ones. Therefore, the critical Euler load taken as a reference for the slender column is no longer valid. In its place the buckling load of a Timoshenko beam-column is considered as reference value (Timoshenko and Gere, 1961):

$$N_{cr,T} = \frac{\sqrt{1 + 4\chi N_{cr,E}/AG} - 1}{2\chi/AG},\qquad(33)$$

where G is the shear modulus and A the cross-sectional area of the column.

The graph in Figure 14 shows the buckling response of the stocky columns for different boundary conditions obtained with HybriDFEM. The curves clearly show convergence to the theoretical Timoshenko beam theory buckling load, indicating that the shear deforma-
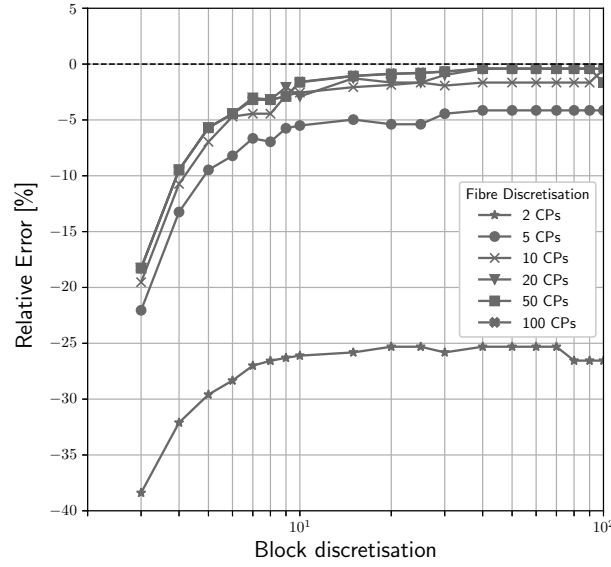
31

Figure 13: Influence of the block size and CP discretisations on the critical buckling load for the pinned-pinned (PP) slender column.

tions are properly taken into account by the model. The error between the computed and estimated Timoshenko buckling load varies between -2.00% (FFr) and -0.00% (FF). The associated buckling modes are visible on the same figure.

3.4. Buckling analysis of systems of blocks

While a very fine block discretisation predicts with precision the buckling load of a continuous column, the present method also enables to model the buckling behaviour of rigid-block assemblies. In this example, a system of two vertically stacked rigid blocks of length $L = 0.5$ m and square cross-section with $h = 0.2$ m, hinged at the bottom and top is considered. A small perturbation consisting in a slight initial rotation of the lower block is introduced by means of a very small moment $M = 10$ Nm applied at the block's centroid, to initiate the nonlinear geometric behaviour, and an axial load is increasingly applied at the top of the stack, by means of a work-control procedure as was done for the continuous columns.
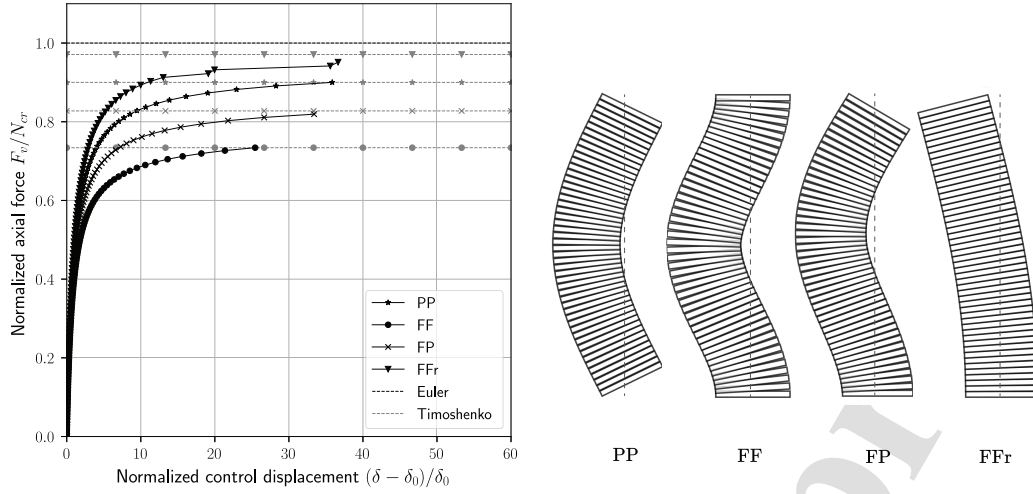
32

Figure 14: Buckling response of a stocky column with different boundary conditions.

The axial stiffness of the interface between the two blocks is distributed in n springs evenly spread across the interface. All springs are assigned an axial stiffness $k_{nn} = 1$ GPa $\cdot$ h/n representing the stiffness of the interface.

Using an equivalent analytical model composed of two 0.5 m rigid bars connected through a rotational spring with stiffness k_r, the buckling load of the stack can be derived (Challamel et al., 2014). For an even number of springs along the interface, its equivalent rotational stiffness equals:

$$k_r = k_{nn} h^3 \frac{1}{2n^3} \sum_{i=1}^{n/2} (2i - 1)^2, \tag{34}$$

The expected buckling load N_{cr} of the analytical model can be derived:

$$N_{cr} = \frac{4k_r}{L} = \frac{2k_{nn}h^3}{L} \frac{1}{n^3} \sum_{i=1}^{n/2} (2i - 1)^2, \tag{35}$$

where $N_{cr} = k_{nn}h^3/4L = 2000$ kN with two CPs, which are located at a distance $h/4$ from the axis of the blocks, and $N_{cr} = k_{nn}h^3/3L = 2667$ kN when the interface is represented by an infinite number of springs, corresponding to the limit for $n \to \infty$ of equation 35. The value of the axial load obtained at the last converged step, with HybriDFEM, for different spring discretisations ranging from 2 springs to 200 springs, are shown in Figure 15 and
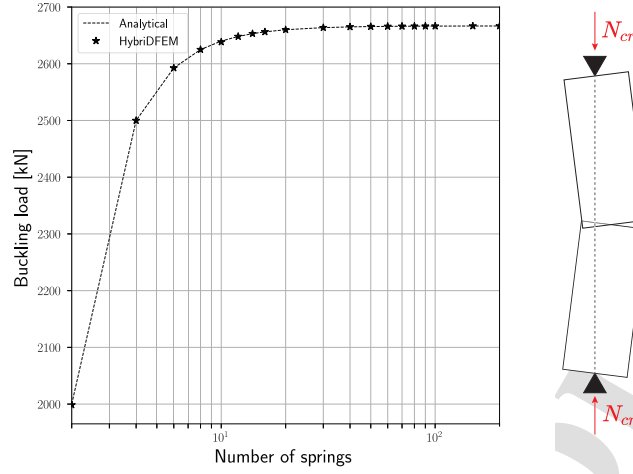
33

Figure 15: Buckling load of two vertically stacked rigid blocks, depending on the number of CPs at the interface.

compared with the analytical value expressed in equation 35, along with the buckling shape of the two blocks. The numerical values show excellent agreement with the analytical ones.

3.5. Flexible column rocking on a rigid foundation

In this benchmark the rocking behaviour of a flexible column on a rigid base is investigated. It shows the ability of the method to capture simultaneously the behaviour of a continuous, flexible column, and the behaviour at the interface between a rigid no-tension support and the flexible column. The benchmark is taken from Avgenakis et al. (Avgenakis and Psycharis, 2017) and consists of a $H = 4$ m-high column with a square cross-section with $h = 1$ m modeled with 40 blocks and 80 CPs per block, and a linear elastic material with $\nu = 0.2$ and values of E varying from 0.3 GPa to 100 GPa. The column is placed on a rigid no-tension support, represented by an additional block fixed in the three directions, to which a linear material law with a very high stiffness E_0 is assigned in compression ($E_0 > 1000E$). Numerically, this corresponds to:

34

$$
\begin{cases}
\sigma = 0 \quad \text{and} \quad \tau = 0 & \text{when} & \varepsilon > 0 \\
\sigma = \varepsilon E_0 & \text{when} & \varepsilon \leq 0
\end{cases}
. \tag{36}
$$

A vertical downwards force $N = 2500$ kN is applied at the top of the column, along with a horizontal force F_h which is controlled by a displacement-control procedure on the top horizontal displacement Δ_h, increased by increments of 5 mm up to 50 cm. Since this problem yields moderate displacements, nonlinear geometric effects are considered.

Considering the column as a rigid block and neglecting its self-weight, nonlinear kinematic analysis yields $F_{h,max} = Nh/2H$ as the force initiating the overturning of the column, and $\Delta_{h,max} = h/2$ as the maximum top displacement, at which the applied axial force no longer opposes the overturning of the column. A curve descending from $(0, F_{h,max})$ to $(\Delta_{h,max}, 0)$ in the $\Delta_h - F_h$-plane, which approaches a straight line for relatively slender columns, represents an envelope curve for all pushover curves obtained for the column when some flexibility is introduced (Giordano et al., 2020). The latter are represented in Figure 16, in which the values of displacement and force are normalized with respect to $F_{h,max}$ and $\Delta_{h,max}$.

The pushover curves of the column obtained for the values of Young's modulus ranging from 0.3 GPa to 100 GPa are visible in Figure 16. The first part of the pushover curves shows a linear behaviour with a stiffer slope for higher values of E. This part corresponds to the column deforming without losing contact with the support. As soon as the overturning is initiated, contacts between the column and the support are lost and the slope of the curve starts decreasing, to finally enter the descending branch of the pushover curve, progressively becoming parallel to the envelope line.

3.6. Coupling with classical FEM

The element presented in this paper has been developed with the intention to couple it with classical finite elements. To illustrate this feature, the benchmark presented hereabove is here reproposed without considering nonlinear geometric effects.
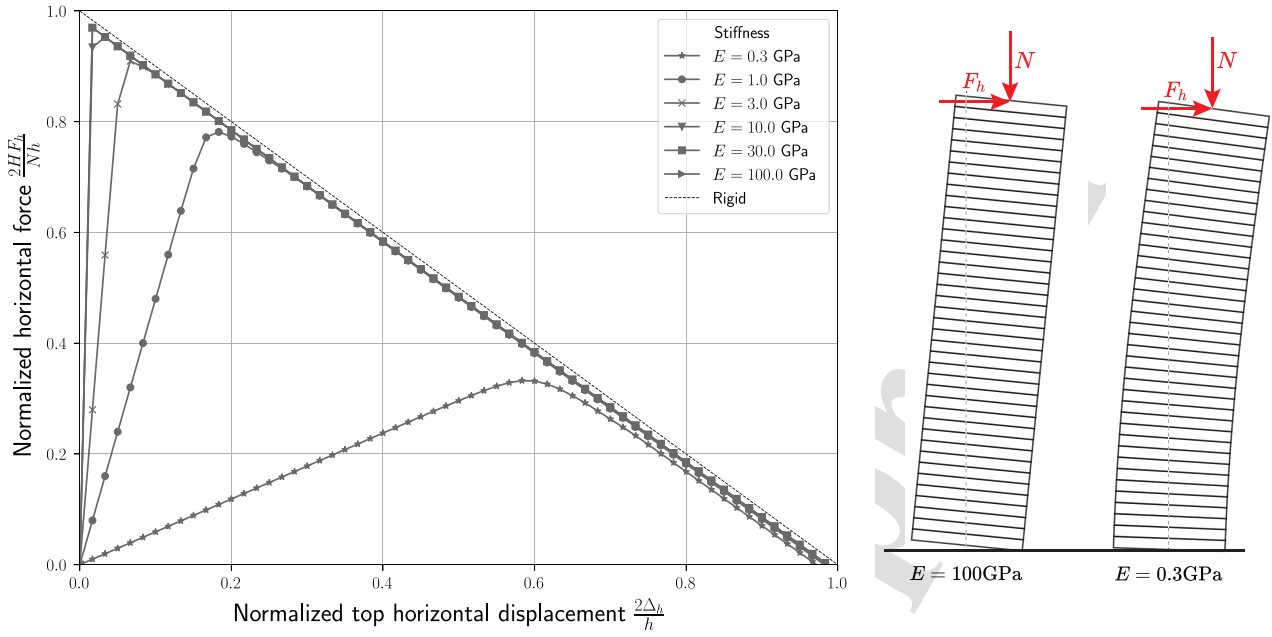
Figure 16: Rocking response of a flexible column on a no-tension rigid foundation.

With reference to Figure 17 (A), two different models have been implemented. The full HybriDFEM model is the same as the one described above, composed of 40 blocks and 80 CPs, except that linear geometry is considered. The HybriDFEM-FEM coupled model is composed of the same support block, followed by ten blocks with 80 CPs representing the first meter of the column. The top block is connected through a rigid-node connection to one linear Timoshenko beam element representing the upper three meters (Davis et al., 1972). The axial and horizontal forces are both applied at the top extremity of the beam finite element. Since the beam element is very simple, in this case one fourth of the height of the column still needed to be modeled with HybriDFEM to allow for a redistribution of the stresses according to Saint Venant's principle.

The two models have been run with a displacement-control procedure up to a normalized top displacement of 1 and the results are compared in Figure 17 (B). The curves associated to the stiffer columns show a very good match between the results of the full HybriDFEM model and the HybriDFEM-FEM coupled model. For the most flexible columns ($E = 0.3$ GPa),
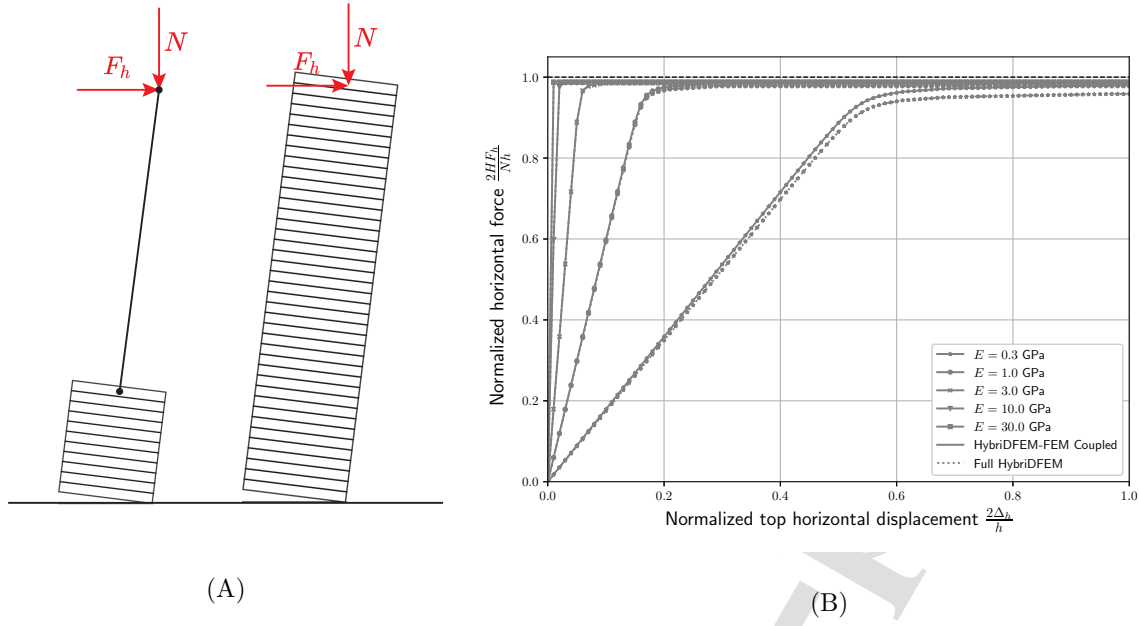
Figure 17: (A) HybriDFEM-FEM coupled and full HybriDFEM model of the column at $\Delta_h = 0.5$ m for $E = 30$ GPa and (B) Normalized force-displacement curves for both models without nonlinear geometric effects.

the response of the coupled model yields a stiffer response than the full HybriDFEM model. On average, the computational time needed for the coupled model was 3.5 to 4 times shorter than for the full model.

4. Conclusions

In this paper, a novel structural analysis method called Hybrid-Discrete-Finite Element Method (HybriDFEM) has been presented. It was developed as a reformulation and extension of the Fibre Contact Element Method (FCEM) (Estêvão and Oliveira, 2015), in which the structure is modeled as a set of rigid blocks connected through nonlinear springs distributed along the contact interfaces. In its current state of development, HybriDFEM can model one-dimensional beam-like elements in which all the blocks are aligned. However, the mathematical developments were carried out anticipating the possibility of having unaligned blocks (e.g. to model curved structures with discontinuities, like masonry arches). Unlike

37

the Applied Element Method (AEM) (Meguro and Tagel-Din, 1999), the interfaces can be composed of multiple springs in series, which allow sectional deformations to be captured or deformations of the interface to be differentiated from deformations of the material. It has been shown that, by adapting the spring constitutive relations, it is possible to model accurately either continuous members or assemblies of distinct blocks as is done in the Discrete Element Methods. Special care has been taken in developing a formulation that resembles the classical FEM, in order to allow for coupling of HybriDFEM with finite elements towards a computationally more efficient model nevertheless able to properly model discontinuities.

In Section 2, the procedure to derive the global resisting forces of the structure was presented step-by-step (Figure 7). This procedure computes the resisting forces in the deformed configuration, thus accounting for nonlinear geometric effects. Moreover, it makes use of an internal nonlinear solution procedure to satisfy equilibrium of the spring forces at the contact points along the interfaces between blocks. Through this iterative solution procedure, nonlinear material behaviour can be accounted for. The internal Newton-Raphson solution procedure was found to converge within a limited number of steps, typically one or two, the only exceptions being when contact between blocks composed of different materials (e.g., a soft block rocking on a rigid base) and moderate displacements (e.g., post-buckling behavior of columns) were analyzed. Consequently, the computational cost associated with this solution scheme, classically adopted in the FEM formulation, is deemed reasonable also in this framework.

After presenting the mathematical derivations of the method, it was validated against benchmark examples (Section 3), demonstrating the performance of the method in modeling continuous planar structures as well as structures presenting discontinuities. Starting from a validation for simple linear elastic beams, its ability to model nonlinear material effects was then demonstrated by modeling the moment-curvature response of a beam with bilinear materials with different hardening and softening ratios. The nonlinear geometric behaviour was validated by modeling the buckling of slender and stocky continuous columns and the buckling of an assembly of two rigid blocks with a flexible interface. Both for the continuous column as for the two rigid blocks, the numerical results showed very good agreement with

the expected analytical values. Then, the rocking behaviour of a flexible column on a rigid base, including nonlinear geometric effects, was validated against the analytical solution of its rigid-block equivalent. Finally, a first example of coupling of HybriDFEM with a classical Timoshenko beam element (Davis et al., 1972) served as a promising proof of concept for the purpose for which the method was developed. This feature will be mainly explored in future works.

Further and ongoing developments of HybriDFEM include the extension to models composed of non-aligned blocks and rigid-node connections to connect different beam-like members, which would allow curved structures and frames with structural discontinuities to be modeled. A time-stepping algorithm will be implemented to handle dynamic problems and model the dynamic collapse of a structure. Extending HybriDFEM to two-directional members (block discretization along perpendicular axes) will allow effects such as the shear stress repartition or St-Venant's principle to be captured. Other promising extensions of the model will also be investigated, namely the coupling of finite elements with HybriDFEM using nonlinear springs instead of rigid-node connections (to model, e.g., detachment), and the use of more advanced FEM formulations (e.g., accounting for geometric and material nonlinearities), towards a computationally efficient approach that fully combines the advantages of FEM with a formulation that explicitly models discontinuities.

5. Acknowledgements

References

Addessi, D., Mastrandrea, A., Sacco, E., 2014. An equilibrated macro-element for nonlinear analysis of masonry structures. Engineering Structures 70, 82–93. doi:10.1016/j.engstruct.2014.03.034.

Applied Science International, L., 2022. Extreme Loading for Structures - 2D 3D Nonlinear Static & Dynamic Structural Analysis Software. Durham, NC, USA. URL: https://www.extremeloading.com/.

Argyris, J., Balmer, H., Doltsinis, J.S., Dunne, P., Haase, M., Kleiber, M., Malejannakis, G.A., Mlejnek, H.P., Müller, M., Scharpf, D., 1979. Finite element method - the natural approach. Computer Methods in Applied Mechanics and Engineering 17-18, 1–106.

Avgenakis, E., Psycharis, I.N., 2017. Modeling of rocking elastic flexible bodies under static loading considering the nonlinear stress distribution at their base. Journal of Structural Engineering 143. doi:10.1061/(asce)st.1943-541x.0001783.

Avgenakis, E., Psycharis, I.N., 2019. Determination of the nonlinear displacement distribution of the semi-infinite strip – application to deformable rocking bodies. International Journal of Solids and Structures 170, 22–37. doi:10.1016/j.ijsolstr.2019.04.030.

Avgenakis, E., Psycharis, I.N., 2020. An integrated macroelement formulation for the dynamic response of inelastic deformable rocking bodies. Earthquake Engineering Structural Dynamics 49, 1072–1094. doi:10.1002/eqe.3279.

Baraldi, D., Bullo, S., Cecchi, A., 2016. Continuous and discrete strategies for the modal analysis of regular masonry. International Journal of Solids and Structures 84, 82–98. doi:10.1016/j.ijsolstr.2016.01.015.

de Borst, R., Crisfield, M.A., Remmers, J.J.C., Verhausel, C.V., 2012. Non-Linear Finite Element Analysis of Solids and Structures. Wiley Series in Computational Mechanics. 2 ed., Chichester.

Bouckaert, I., Godio, M., Pacheco de Almeida, J., 2021. Large-displacement response of unreinforced masonry structures: comparison between analytical solutions and dem models including open-source software, in: COMPDYN - 8th ECCOMAS Thematic Conference on Computational Methods in Structural Dynamics and Earthquake Engineering, p. 15.

Bouckaert, I., Godio, M., Pacheco de Almeida, J., 2022. A strategy for generating pushover curves of block assemblies including post-peak branch using the discrete element method, in: 3ECEES - Third European Conference on Earthquake Engineering and Seismology.

Casolo, S., Uva, G., 2013. Nonlinear analysis of out-of-plane masonry façades: full dynamic versus pushover methods by rigid body and spring model. Earthquake Engineering Structural Dynamics 42, 499–521. doi:10.1002/eqe.2224.

Cecchi, A., Tralli, A., 2012. A homogenized viscoelastic model for masonry structures. International Journal of Solids and Structures 49, 1485–1496. doi:10.1016/j.ijsolstr.2012.02.034.

Challamel, N., Wang, C.M., Elishakoff, I., 2014. Discrete systems behave as nonlocal structural elements: Bending, buckling and vibration analysis. European Journal of Mechanics - A/Solids 44, 125–135. doi:10.1016/j.euromechsol.2013.10.007.

Chetouane, B., Dubois, F., Vinches, M., Bohatier, C., 2005. NSCD discrete element method for modelling masonry structures. International Journal for Numerical Methods in Engineering 64, 65–94. doi:10.1002/nme.1358.

Crisfield, M.A., 1990. A consistent co-rotational formulation for non-linear, three-dimensional, beam-elements. Computer Methods in Applied Mechanics and Engineering 81, 131–150.

Cundall, P.A., 1971. A computer model for simulating progressive large scale movements in blocky rock systems, in: Symposium of the International Society for Rock Mechanics, Society for Rock Mechanics (ISRM).

Davis, R., Henshell, R.D., Warburton, G.B., 1972. A timoshenko beam element. Journal of Sound and Vibration 33, 475–487.

Dubois, F., Acary, V., Jean, M., 2018. The contact dynamics method: A nonsmooth story. Comptes Rendus Mécanique 346, 247–262. URL: https://dx.doi.org/10.1016/j.crme.2017.12.009, doi:10.1016/j.crme.2017.12.009.

Estêvão, J.M.C., Carreira, A.S., 2015. Using the new fibre contact element method for dynamic structural analysis. Engineering Structures and Technologies 7, 24–38. doi:10.3846/2029882x.2015.1087346.

Estêvão, J.M.C., Oliveira, C.S., 2015. A new analysis method for structural failure evaluation. Engineering Failure Analysis 56, 573–584. doi:10.1016/j.engfailanal.2014.08.009.

Gatta, C., Addessi, D., Vestroni, F., 2018. Static and dynamic nonlinear response of masonry walls. International Journal of Solids and Structures 155, 291–303. doi:10.1016/j.ijsolstr.2018.07.028.

Giordano, N., De Luca, F., Sextos, A., 2020. Out-of-plane closed-form solution for the seismic assessment of unreinforced masonry schools in nepal. Engineering Structures 203. doi:10.1016/j.engstruct.2019.109548.

Itasca, 2022. UDEC 7.0. Minneapolis, USA. URL: https://www.itascacg.com/software/udec/.

Itasca, 2023. 3DEC 7.0. Minneapolis, USA. URL: https://www.itasca.fr/software/3DEC.

Jean, M., 1995. Frictional contact in collections of rigid or deformable bodies: numerical simulation of geomaterial motions. Mechanics of Geomaterial Interfaces , 463.

Jean, M., 1999. The non-smooth contact dynamics method. Computer Methods in Applied Mechanics and Engineering 177, 235–257. URL: https://dx.doi.org/10.1016/s0045-7825(98)00383-1, doi:10.1016/s0045-7825(98)00383-1.

Lagomarsino, S., Penna, A., Galasco, A., Cattari, S., 2013. Tremuri program: An equivalent frame model for the nonlinear seismic analysis of masonry buildings. Engineering Structures 56, 1787–1799. doi:10.1016/j.engstruct.2013.08.002.

Lemos, J., 2019. Discrete element modeling of the seismic behavior of masonry construction. Buildings 9, 43. URL: https://dx.doi.org/10.3390/buildings9020043, doi:10.3390/buildings9020043.

Lemos, J.V., 2007. Discrete elements modeling of masonry structures. International Journal of Architectural Heritage .

Lourenço, P.B., 1996. Computational Strategies for Masonry Structures. Thesis.

Lourenço, P.B., Rots, J.G., Blaauwendraad, J., 1998. Continuum model for masonty: parameter estimation

and validation. Journal of Structural Engineering .

Malomo, D., Pinho, R., Penna, A., 2018. Using the applied element method for modelling calcium silicate brick masonry subjected to in-plane cyclic loading. Earthquake Engineering Structural Dynamics 47, 1610–1630. doi:10.1002/eqe.3032.

Malomo, D., Scattarreggia, N., Orgnoni, A., Pinho, R., Moratti, M., Calvi, G.M., 2020. Numerical study on the collapse of the morandi bridge. Journal of Performance of Constructed Facilities 34. doi:10.1061/(asce)cf.1943-5509.0001428.

Mark, R., Cakmak, A.S., Erdik, M., 1993. Modelling and monitoring the structure of hagia sophia in istanbul. IABSE reports 70. doi:10.5169/seals-53293.

Meguro, K., Tagel-Din, H., 1999. Simulation of buckling and post-buckling behavior of structures using applied element method. Bull. ERS 32.

Meguro, K., Tagel-Din, H., 2000. Applied element method for structural analysis: Theory and application for linear materials. J. Struct. Mech. Earthquake Eng. 647.

Moes, N., Dolbow, J., Belytschko, T., 1999. A finite element method for crack growth without remeshing. International Journal for Numerical Methods in Engineering 46, 131–150. doi:10.1002/(sici)1097-0207(19990910)46:1<131::Aid-nme726>3.0.Co;2-j.

Munjiza, A., Latham, J.P., 2002. Computational challenge of large scale discontinua analysis. Third International Conference on Discrete Element Methods .

Orduña, A., 2017. Non-linear static analysis of rigid block models for structural assessment of ancient masonry constructions. International Journal of Solids and Structures 128, 23–35. doi:10.1016/j.ijsolstr.2017.07.022.

Pandit, D., Srinivasan, S.M., 2016. An incremental approach for springback analysis of elasto-plastic beam undergoing contact driven large deflection. International Journal of Mechanical Sciences 115-116, 24–33. doi:10.1016/j.ijmecsci.2016.06.003.

Pecker, A., Chatzigogos, C.T., Salençon, J., 2010. A dynamic macro-element for performance-based design of foundations. Advances in Performance-Based Earthquake Engineering , 103–112.

Pegon, P., Pinto, A.V., Anthoine, A., 1995. Numerical simulation of historical buildings subjected to earthquake loading. Transactions on the Built Environment 15.

Penna, A., Lagomarsino, S., Galasco, A., 2014. A nonlinear macroelement model for the seismic analysis of masonry buildings. Earthquake Engineering Structural Dynamics 43, 159–179. doi:10.1002/eqe.2335.

Portioli, F., Casapulla, C., Cascini, L., 2015. An efficient solution procedure for crushing failure in 3d limit analysis of masonry block structures with non-associative frictional joints. International Journal of Solids and Structures 69-70, 252–266. doi:10.1016/j.ijsolstr.2015.05.025.

Portioli, F.P.A., 2020. Rigid block modelling of historic masonry structures using math-

ematical programming: a unified formulation for non-linear time history, static pushover and limit equilibrium analysis. Bulletin of Earthquake Engineering 18, 211–239. URL: https://dx.doi.org/10.1007/s10518-019-00722-0, doi:10.1007/s10518-019-00722-0.

Pulatsu, B., Erdogmus, E., Lourenço, P.B., Lemos, J.V., Tuncay, K., 2020. Simulation of the in-plane structural behavior of unreinforced masonry walls and buildings using dem. Structures 27, 2274–2287. doi:10.1016/j.istruc.2020.08.026.

Roca, P., Cervera, M., Gariup, G., Pela', L., 2010. Structural analysis of masonry historical constructions. classical and advanced approaches. Archives of Computational Methods in Engineering 17, 299–325. doi:10.1007/s11831-010-9046-1.

Rust, W., 2015. Non-Linear Finite Element Analysis in Structural Mechanics. doi:DOI 10.1007/978-3-319-13380-5.

Sarhosis, V., Bagi, K., Lemos, J.V., Gabriele, M., 2016. Computational Modeling of Masonry Structures Using the Discrete Element Method. Advances in Civil and Industrial Engineering (ACIE), Engineering Science Reference, Hershey PA, USA.

Scattarreggia, N., Malomo, D., DeJong, M.J., 2022. A new distinct element meso-model for simulating the rocking-dominated seismic response of rc columns. Earthquake Engineering Structural Dynamics 52, 828–838. doi:10.1002/eqe.3782.

Smoljanović, H., Živaljić, N., Nikolić, ., Munjiza, A., 2018. Numerical analysis of 3d dry-stone masonry structures by combined finite-discrete element method. International Journal of Solids and Structures 136-137, 150–167. doi:10.1016/j.ijsolstr.2017.12.012.

Stephen, N.G., 1997. Mindlin plate theory:best shear coefficient and higher spectra validity. Journal of Sound and Vibration 202, 539–553.

Swati, R.F., Wen, L.H., Elahi, H., Khan, A.A., Shad, S., 2018. Extended finite element method (xfem) analysis of fiber reinforced composites for prediction of micro-crack propagation and delaminations in progressive damage: a review. Microsystem Technologies 25, 747–763. doi:10.1007/s00542-018-4021-0.

Taforel, P., 2012. Apport de la Méthode des Eléments Discrets à la Modélisation des Maçonneries en Contexte Sismique : Vers une Nouvelle Approche Numérique de la Vulnérabilité Sismique. Thesis.

Tagel-Din, H., Meguro, K., 1999. Applied element simulation for collapse analysis of structures. Bull. ERS 32.

Tagel-Din, H., Meguro, K., 2000. Nonlinear simulation of rc structures using applied element method. J. Struct. Mech. Earthquake Eng. 654.

Timoshenko, S., Gere, J.M., 1961. Theory of Elastic Stability. 2nd edition ed., Dover Publications, Mineola, N. Y.

UMontpellier, 2023. LMGC90 User version. Montpellier, France. URL:

https://git-xen.lmgc.univ-montp2.fr/lmgc90/lmgc90_user.

Zhang, S., Taheri Mousavi, S.M., Richart, N., Molinari, J.F., Beyer, K., 2017. Micro-mechanical finite element modeling of diagonal compression test for historical stone masonry structure. International Journal of Solids and Structures 112, 122–132. doi:10.1016/j.ijsolstr.2017.02.014.

Declaration of interests

☒ The authors declare that they have no known competing financial interests or personal relationships that could have appeared to influence the work reported in this paper.

☐The authors declare the following financial interests/personal relationships which may be considered as potential competing interests: